

The Millennium and Astrid galaxies in effective field theory: comparison with galaxy-halo connection models at the field level

Mikhail M. Ivanov,^{1,2,*} Carolina Cuesta-Lazaro,^{2,3,4,†} Andrej Obuljen,⁵ Michael W. Toomey,¹ Yueying Ni,⁴ Sownak Bose,⁶ Boryana Hadzhiyska,^{7,8,9} César Hernández-Aguayo,^{10,11} Lars Hernquist,⁴ Rahul Kannan,¹² and Volker Springel¹⁰

¹*Center for Theoretical Physics, Massachusetts Institute of Technology, Cambridge, MA 02139, USA*

²*The NSF AI Institute for Artificial Intelligence and Fundamental Interactions, Cambridge, MA 02139, USA*

³*Department of Physics, Massachusetts Institute of Technology, Cambridge, MA 02139, USA*

⁴*Center for Astrophysics | Harvard & Smithsonian, 60 Garden St, Cambridge, MA 02138, USA*

⁵*Department of Astrophysics, University of Zurich,
Winterthurerstrasse 190, 8057 Zurich, Switzerland*

⁶*Institute for Computational Cosmology, Department of Physics,
Durham University, South Road, Durham, DH1 3LE, UK*

⁷*Miller Institute for Basic Research in Science, University of California, Berkeley, CA, 94720, USA*

⁸*Physics Division, Lawrence Berkeley National Laboratory, Berkeley, CA 94720, USA*

⁹*Berkeley Center for Cosmological Physics, Department of Physics,
University of California, Berkeley, CA 94720, USA*

¹⁰*Max-Planck-Institut für Astrophysik, Karl-Schwarzschild-Str. 1, D-85748, Garching, Germany*

¹¹*Excellence Cluster ORIGINS, Boltzmannstrasse 2, D-85748 Garching, Germany*

¹²*Department of Physics and Astronomy, York University,
4700 Keele Street, Toronto, ON M3J 1P3, Canada*

Cosmological analyses of redshift space clustering data are primarily based on using luminous “red” galaxies (LRGs) and “blue” emission line galaxies (ELGs) to trace underlying dark matter. Using the large high-fidelity high-resolution MillenniumTNG (MTNG) and Astrid simulations, we study these galaxies with the effective field theory (EFT)-based field level forward model. We confirm that both red and blue galaxies can be accurately modeled with EFT at the field level and their parameters match those of the phenomenological halo-based models. Specifically, we consider the state of the art Halo Occupation Distribution (HOD) and High Mass Quenched (HMQ) models for the red and blue galaxies, respectively. Our results explicitly confirm the validity of the halo-based models on large scales beyond the two-point statistics. In addition, we validate the field-level HOD/HMQ-based priors for EFT full-shape analysis. We find that the local bias parameters of the ELGs are in tension with the predictions of the LRG-like HOD models and present a simple analytic argument explaining this phenomenology. We also confirm that ELGs exhibit weaker non-linear redshift-space distortions (“fingers-of-God”), suggesting that a significant fraction of their data should be perturbative. We find that the response of EFT parameters to galaxy selection is sensitive to assumptions about baryonic feedback, suggesting that a detailed understanding of feedback processes is necessary for robust predictions of EFT parameters. Finally, using neural density estimation based on paired HOD-EFT parameter samples, we obtain optimal HOD models that reproduce the clustering of Astrid and MTNG galaxies.

1. INTRODUCTION

Observations of clustering of galaxies on large cosmological scales is a key source of information about the

constitution, expansion history, and initial conditions of our Universe. The growing importance of galaxy clustering is reflected by investments into current and future surveys such as DESI [1], Euclid [2], LSST [3], and Roman [4]. Realizing the potential of these surveys’ data requires an understanding of main galaxies used to map our Universe. For the current and near-term future surveys the most common types are red luminous galaxies

* ivanov99@mit.edu

† cuestalz@mit.edu

(LRGs) and emission line galaxies (ELGs), often dubbed simply as red and blue galaxies, respectively [5, 6].

The most accurate way to understand fundamental cosmological properties of galaxies is to rely on first-principle hydrodynamical (hydro) simulations, which self-consistently solve the coupled equations for the evolution of gas and dark matter. Relatively recently hydrodynamical simulations have become large enough to allow for precision studies of large-scale clustering properties relevant for cosmological analyses [7–9]. A computationally inexpensive alternative to complete hydro simulations is given by empirical prescriptions to “paint” galaxies onto dark matter halos. Such empirical models of the galaxy-halo connection, such as halo occupation distribution (HOD) [10–12] or the subhalo abundance matching (SHAM) [13] (see [14] for review), allow for an efficient statistical description of basic clustering observables. The HOD models were originally developed for the description of red galaxies, and then later extended to the blue galaxies in [15–17].

On very large, quasi-linear scales, one can use the perturbative bias expansion to model the galaxy density field, see [18] for a review. The perturbative techniques have recently experienced a revival of interest spurred by the development of the effective field theory (EFT) of large-scale structure [19–21] in its various formulations [22–24], and their successful application in extraction of cosmological parameters from the galaxy clustering data [25–31]. Although EFT applies only on quasi-linear scales, it relies only on symmetries and dimensional analysis, and hence is largely agnostic about the galaxy formation physics on small scales. EFT captures different types of galaxies by means of the EFT bias parameters, see [18] for a review. The EFT parameters can be predicted in a given model of the galaxy distribution, such as HOD or the hydro simulation. This knowledge can be used to inform priors on EFT parameters in the EFT-based data analyses. Early examples of a similar approach applied in perturbation theory based galaxy clustering analyses can be found in e.g. [32–34]. This idea has been recently amalgamated into the EFT-based full-shape analysis with HOD-based priors based on neural density estimation, developed and applied to data in [35, 36], see also [37, 38]. This approach makes use of the field-level EFT technique [39–54], which enables one to cancel cosmic variance and thus achieve a high precision of EFT parameter measurements from small simu-

lation volumes.¹ The HOD-based priors lead to substantial improvements of the cosmological constraints [35, 36]. The increased statistical power calls for the validation of the HOD-based priors with the results of the *ab initio* galaxy modeling from hydrodynamic simulations.

The hydro galaxies from the IllustrisTNG simulation [8] have been studied in the context of the field-level EFT models in refs. [50, 57]. These works measured relations between the bias parameters of the hydro galaxies and compared them with those of dark matter halos. In this work we build on results of [50, 57] and extend them by (a) utilizing the large volume high-fidelity MillenniumTNG (MTNG) simulation [58] which provides a higher precision than IllustrisTNG, (b) comparing the bias parameters of the hydro galaxies with those of the state-of-the-art halo models with assembly bias, and (c) focusing specifically on the red and blue galaxies that closely match those observed in actual surveys such as BOSS [59] and DESI [6].

In addition to MTNG, we analyze galaxies from the large volume high resolution Astrid simulation [60, 61]. Astrid uses a galaxy formation model different from MTNG, with many unique features associated with both the low and high redshift physics. In particular, Astrid has a different active galaxy nucleus (AGN) implementation. Thus, the comparison of MTNG and Astrid results will allow us to estimate the sensitivity of EFT parameters to the underlying galaxy formation scenario.

Another motivation for our study is to test the accuracy of the HOD modeling for the red and blue hydro galaxies at the field level. In terms of the actual clustering observables, the HOD and hydro galaxies have been extensively compared in the past at the level of the two-point function [62–65] and the squeezed limit of the three-point function [66]. In this work, we confront the two approaches at the field level, albeit only on large scales where the two can be connected via their EFT parameters.

The halo-based models have been utilized in various simulation-based analyses, e.g. in a recent community data challenge “Beyond-2pt” [67], see also [68–73]. The success of simulation-based techniques in this challenge

¹ Achieving a similar precision with the clustering observables, such as the power spectrum and bispectrum requires significantly larger simulation volumes, $\sim 600 [h^{-1}\text{Gpc}]^3$ [55, 56].

calls for additional tests of the HOD modeling at the field level. Such tests are especially important for ELGs, which are less understood than the red galaxies. Even in the context of perturbation theory, the ELGs have been studied only at the level of the two-point function and only for HOD-based simulations [74–77]. Importantly, these analyses showed that these galaxies feature a weaker fingers-of-God signature than the LRGs, which could extend the validity of the perturbative regime for them and hence provide tighter cosmological constraints [56, 76, 78, 79]. This observation calls for a further validation against the high quality hydrodynamic galaxies, which we present here.

From the galaxy-halo connection side, we use the baseline modified High Mass Quenched (HMQ) model for ELGs adopted by DESI [80, 81], which is built on [15–17, 82]. We create samples of EFT parameters following the same approach as [35, 36], and compare them against the measurements from blue galaxies of MTNG and Astrid simulations.

Our paper is structured as follows. We present the main results in Section 2. Our methodology, EFT and HOD modeling, and data are discussed in Section 3. Section 4 describes our analysis and results in detail. There we compare the EFT parameters of hydrodynamic galaxies with the HOD-based priors. Section 5 draws conclusions.

2. MAIN RESULTS

Let us start with the summary of our methodology and main results. We extract EFT parameters of BOSS and DESI-like LRGs at $z = 0.5$ and ELGs at $z = 1$ from MTNG and Astrid simulations. We consider several different LRG and ELG selections. Specifically, following [62–65], we use the cuts on the number density (equivalent to the stellar mass) and the specific star formation rate (sSFR), i.e. the star formation rate normalized by the galaxy’s stellar mass. We use $h\text{-yr}^{-1}$ units for sSFR. Physically sSFR^{-1} is the typical timescale over which the stellar mass doubles.

We measure EFT parameters by fitting the transfer functions of the field-level model of [43, 49] following the approach of [35, 36].² Our measurements of the real-

space EFT parameters for DESI-like LRGs and ELGs are displayed in figs. 1, 2 respectively. Our main findings are:

1. Consistency of hydro-based EFT parameters with HOD values for LRGs. We have found all EFT parameter values for LRGs are highly consistent with the HOD-based values from the decorated models considered in refs. [35, 36], see fig. 1. This confirms that the HOD priors from these works are robust under the variation of the underlying galaxy distribution model. Our results also explicitly confirm the validity of the LRG-HOD models beyond the two point function statistic, albeit only on quasilinear scales.

We have also confirmed previous reports [36, 55, 83] that the quadratic bias parameters b_2 for LRG-HOD are larger than those of the dark matter halos [84] for $b_1 \sim 2$. We also show that this behavior naturally follows from the shape of the LRG-HOD function and the dark matter halo mass function.

2. Modeling ELGs at the field level. We have carried out precision measurements of the full set of EFT parameters for ELGs at the field level for the first time. Our results agree with previous analyses based on the eBOSS ELG data [75, 76] and the early ELG-halo based models [15, 85]. Our measurements of EFT parameters can be used to inform and validate full-shape analyses of the DESI ELGs [77].

3. Local bias parameters of ELGs. One interesting outcome of our measurements is that ELG’s combinations of local (in matter density) bias parameters $\{b_1, b_2, b_3\}$ appear to be in a very strong tension with the HOD values when using the LRG-based halo models. There is no (decorated) HOD model for LRGs that can reproduce the combination of large-scale local bias parameters of ELGs. This is expected from the phenomenological point of view as the blue galaxies quench at late stages of their evolution (after undergoing a few mergers) and no longer produce strong emission lines.

In contrast to the local bias parameters, the other EFT parameters of ELGs beyond the local ones appear very similar to the LRG-HOD ones. This means that one can, in principle, reproduce non-local EFT parameters of ELGs with an appropriate choice of parameters of the LRG-HOD models. The non-LRG-like distribution of the

² These are produced with the code `Hi-Fi mocks` publicly available

at https://github.com/andrejobuljen/Hi-Fi_mocks.

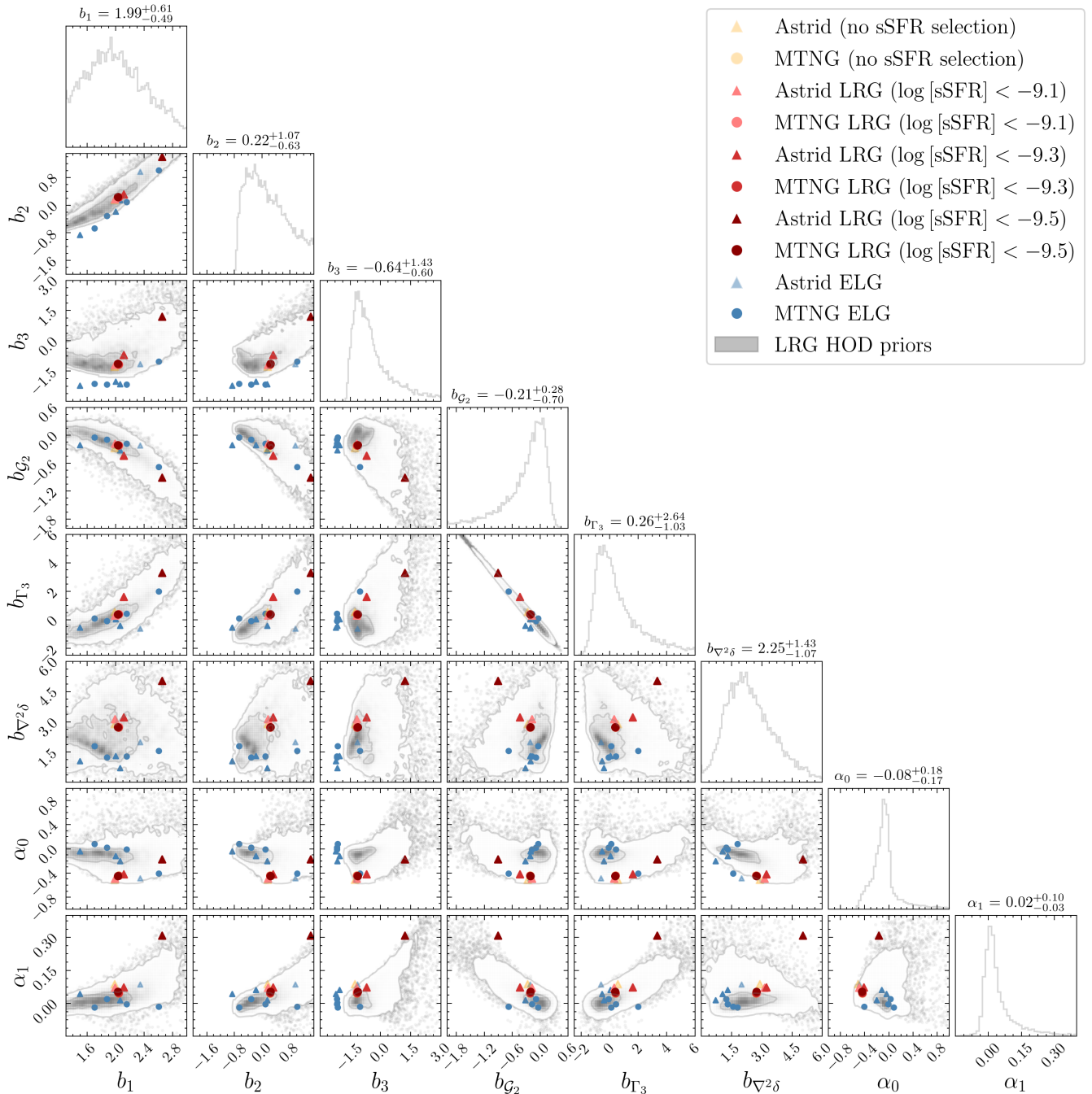


FIG. 1. MTNG and Astrid bias parameters for LRGs against the LRG-HOD-based density distribution (LRG-HOD priors). For comparison, we also show four ELGs samples.

local bias coefficients is an interesting signature of ELGs, which we show to directly follow from their halo occupation shape.

In contrast to the $\{b_1, b_2\}$ values of LRG-HOD galaxies, the local ELG bias parameters that we have measured are consistent with those of the underlying dark matter halos. We present a simple analytic argument explain-

ing this phenomenology. It will be interesting to develop more sophisticated semi-analytic models of ELGs along the lines of [86].

4. Consistency of HMQ models with hydro galaxies at the field level. To extend the simulation based prior approach to ELGs we have generated a large sample of EFT parameters using 10500 synthetic cat-

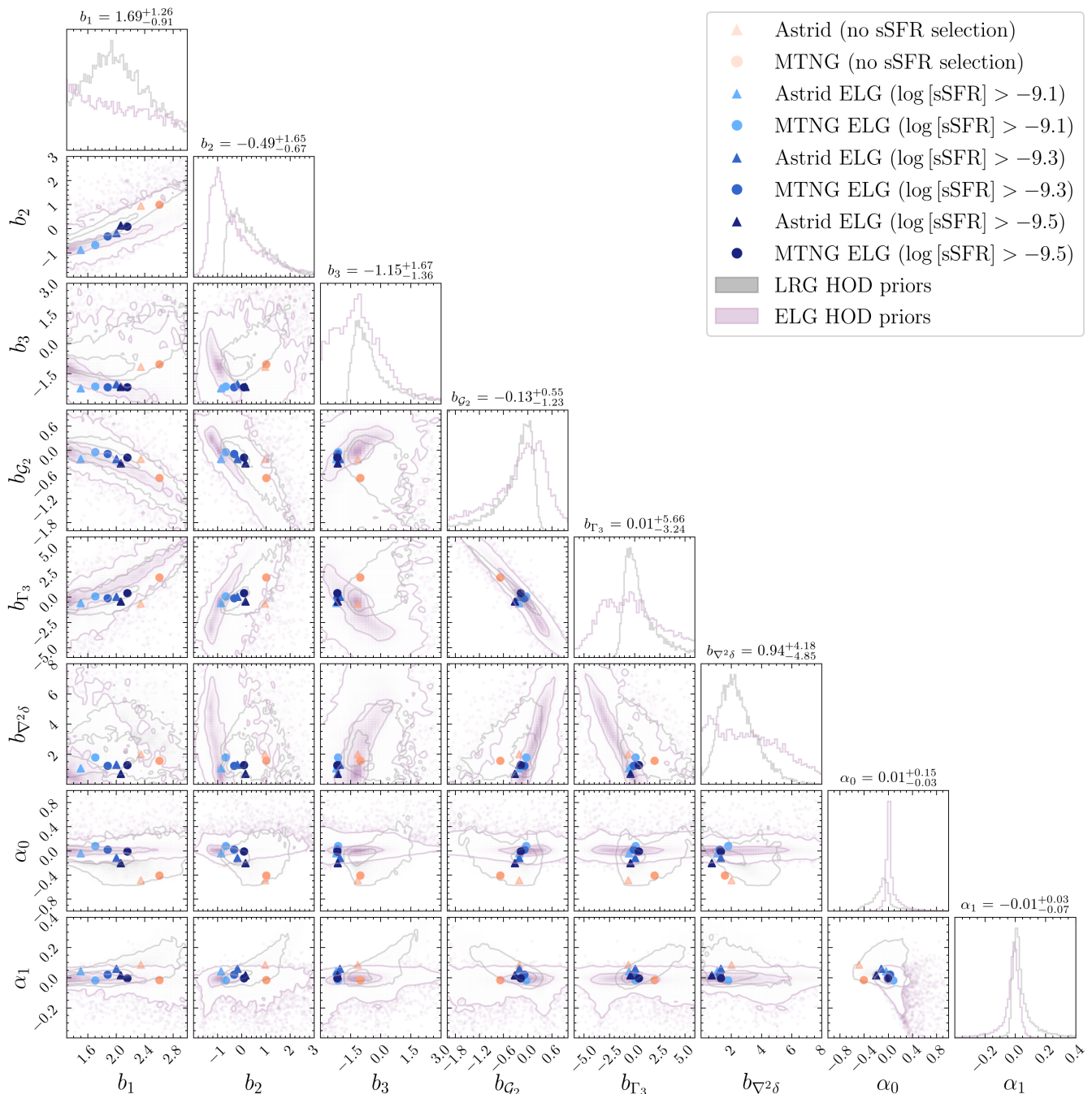


FIG. 2. MTNG and ASTRID bias parameters of ELGs vs. the distributions extracted from LRG-based HOD and ELG-based HMQ catalogs.

alogs based on the phenomenological HMQ model. We have shown that the HMQ model captures well the above “anomalous” behavior of the local bias parameters, see fig. 2. It also correctly reproduces the weaker fingers-of-God signature observed for the ELGs. Therefore, our analysis confirms the validity of the HMQ model at the field level (albeit only on large scales). Thus, our work

supports validation studies of the HMQ model based on the two-point functions (e.g. [80]) and extends them to higher-order clustering observables.

5. Weak non-linear redshift-space distortions of ELGs. We have found that ELG from the hydrodynamic simulations feature weaker non-linear redshift-space distortions, known as the “fingers-of-God” (FOG) [87]. This

signature is well reproduced by the HMQ models: the distribution of the EFT redshift-space counterterms from these models is significantly narrower than that of LRG-HOD. If this is an actual physical property of the ELG in our Universe, it can have a profound impact on the perturbative analyses of ELG samples. Weaker FOG imply a larger cutoff scale of EFT, thereby increasing k_{max} in cosmological analyses and yielding more data in the perturbative regime [56, 76, 78, 79].

From the physical perspective, weaker FOG follow from the fact that ELGs reside in small mass host halos which have a relatively low (i.e. “cold”) velocity dispersion.

6. The response of the EFT parameters to the specific star formation rate. We have studied the dependence of the EFT parameters on galaxy selection. We find that the response of Astrid and MTNG LRGs to sSFR is quite different. The EFT parameters of MTNG LRGs respond to sSFR very weakly³, while for Astrid we observe some noticeable response whose strength grows for smaller sSFR cuts. In terms of the EFT parameter values, the results of Astrid and MTNG are broadly consistent for LRGs selected with sSFR thresholds corresponding to fast star formation. However, Astrid and MTNG predict quite different LRGs if we apply more realistic sSFR cuts consistent with slow star formation. In this case Astrid galaxies live in more massive halos, which results in larger values of EFT bias parameters. We argue that the discrepancy between the LRG sSFR responses can be explained by the difference in the MTNG and Astrid feedback models. Specifically, in the context of the sSFR sensitivity, the most relevant feedback parameters are AGN response, gas cooling, star formation, and quenching mechanisms.

For ELGs, Astrid and MTNG galaxies are quite consistent as functions of sSFR, and they both predict a strong dependence on sSFR thresholds. The exact form of the response is however slightly different, which again, can be traced back to the differences in feedback.

Finally, let us note that the simulation-based prior approach proposed in [35, 36] can be applied to hydrodynamic simulations as well. This will require producing a suite of simulations with different subgrid models, similar to CAMELS [88], but in a cosmologically large volume.

7. Optimal galaxy-halo connection for hydrodynamic galaxies via EFT parameters. The HOD priors for EFT parameters from [35, 36] can be used to map the bias parameters onto HOD models via a conditional distribution modeled with normalizing flows. Then, the EFT parameters of hydrodynamic galaxies can be used to predict optimal values of HOD parameters that are needed to reproduce the large-scale clustering of hydro galaxies within the HOD framework. This approach is based only on using the large-scale clustering information, but it allows for an efficient, cheap, and accurate matching of the clustering observables at the field level. This approach may be useful for calibration of HOD models at the field level.

We realize this idea in practice and explicitly present HOD/HMQ models needed to reproduce the clustering of hydro galaxies with the target EFT parameters from Astrid and MTNG. The optimal halo model parameters we find are consistent with halos hosting the hydro galaxies.

3. METHODOLOGY

The main goal of this work is to measure EFT parameters of the BOSS-like and DESI-like hydro galaxies and compare them with those of the HOD/HMQ based galaxies. To extract the EFT parameters at high precision, we use the field-level EFT forward model which allows for cosmic variance cancellation. Let us describe now the simulations that we use here, the galaxy selection, the HOD models, and the field-level EFT technique.

3.1. Hydrodynamic Simulations

We start with a brief description of the hydrodynamic simulations studied in this work.

MTNG. We use the largest hydrodynamic box MTNG740 with $500 h^{-1}\text{Mpc}$ side length. This box contains 2×4230^3 resolution elements. MTNG is based on the underlying cosmology of the IllustrisTNG simulation: $\{\Omega_m, \Omega_b, h, \sigma_8, n_s, M_\nu/\text{eV}\} = \{0.3089, 0.0486, 0.6774, 0.8159, 0.9667, 0\}$, where Ω_m, Ω_b are late-time abundances of matter and baryons, h is the reduced Hubble constant, σ_8 is the mass fluctuation amplitude, n_s is the primordial spectral tilt, and M_ν is the total neutrino mass.

³ It is consistent with results for IllustrisTNG [57].

The key feature of MTNG that is crucial for our study is the large volume, providing small statistical errors, which is crucial for accurate measurements of the large-scale EFT parameters. The MTNG simulation is based on the physics model detailed in [8, 89–95]. We refer the reader to [9, 58] for further technical details and outputs of the MTNG simulation.

Astrid. In addition to MTNG, we also include another cosmological galaxy formation simulation Astrid [60] as a complementary study. Astrid is conducted within a $250 h^{-1}\text{Mpc}$ box with 2×5500^3 particles, achieving a baryon mass resolution of $\sim 10^6 M_\odot$. This allows Astrid to resolve galaxies and halos down to lower mass scales, though it introduces larger statistical scatter on large scales. The cosmological parameter employed by Astrid are based on [96]: $\{\Omega_m, \Omega_b, h, \sigma_8, n_s, M_\nu/\text{eV}\} = \{0.3089, 0.0486, 0.6774, 0.816, 0.9667, 0.06\}$.

The Astrid galaxy formation model is described in detail in [60]. In particular, gas cools via primordial radiative cooling [97] and metal-line cooling, with gas and stellar metallicities evolving according to the prescriptions in [98]. The simulation adopts patchy reionization [99] and employs the ionizing UV background from [100], along with gas self-shielding [101]. Star formation follows a multi-phase model [102] that accounts for the influence of molecular hydrogen [103]. Feedback from Type II supernovae is implemented following [104], with wind speeds proportional to the local dark matter velocity dispersion. Black hole seeding, accretion, feedback, and dynamics are modeled as described in [105].

3.2. Galaxy populations

MTNG. We select samples that are similar to BOSS LRGs, DESI LRGs, DESI ELGs catalogs. The redshifts of the samples are $z = 0.5$ for LRGs and $z = 1$ for ELGs. ELGs and LRGs are selected by applying specific star formation cuts following [62–65], at a fixed target number density. The SFR cut selection provides a good approximation to samples of [OII] emitting galaxies. A more robust way to identify emission line galaxies is to model the colors and emission lines in detail with a population synthesis model. However, as shown in [62], a careful color modeling with population synthesis and matching to color-color data consistent with the DESI observations produces results similar to the ones coming

from the sSFR-selection.

In our selection, the total stellar mass is adjusted to reproduce the target number density, which is equivalent to applying stellar mass cuts as in [62]. The BOSS/DESI samples have number densities $3.5 \times 10^{-4} [h^{-1}\text{Mpc}]^{-3}$ and $5 \times 10^{-4} [h^{-1}\text{Mpc}]^{-3}$, respectively. All ELG samples have the DESI-like number density $5 \times 10^{-4} [h^{-1}\text{Mpc}]^{-3}$ [6, 80].

For each number density choice we consider four different sub-samples: all galaxies, and three samples whose specific star formation rate (sSFR) is lower than a fixed threshold. Physically, sSFR^{-1} is the typical timescale over which the stellar mass in the galaxy doubles due to active star formation. It is convenient to use the variable $\tau_{\text{sSFR}} = -\log_{10}(\text{sSFR}/(h \cdot \text{yr}^{-1}))$, i.e. the logarithm of this time scale. Larger values of τ_{sSFR} imply slower star mass accumulation. The sSFR thresholds for LRGs we consider are $\tau_{\text{sSFR}} = 9.0862$, $\tau_{\text{sSFR}} = 9.2596$, and $\tau_{\text{sSFR}} = 9.5376$. Our selection for one fixed sSFR cut is illustrated in Fig. 3. Note that “all galaxies” implies no sSFR cut whatsoever, and hence this sample contains both LRGs and ELGs. Fig. 3 shows that this sample is, however, largely dominated by LRGs. Also note that [64] used $\tau_{\text{sSFR}} = 9.0862$ as a baseline choice.

Following [64], ELGs are selected by applying the specific star formation rate cut $\tau_{\text{sSFR}} = 9.0862$. This should be treated as a baseline choice of ELG selection. In addition, we consider two higher τ_{sSFR} , i.e. smaller star formation rates, $\tau_{\text{sSFR}} = 9.2596$, and $\tau_{\text{sSFR}} = 9.5376$, and also a sample of all galaxies. Note that we do not expect that the latter three samples match the DESI galaxies well, especially the “All” samples that do not apply any sSFR cut, and which are actually dominated by LRGs. Nevertheless, bracketing the sSFR values provides an insight into the sensitivity of the ELG clustering to the applied sSFR cuts.

Astrid. For LRGs and ELGs, we implement the selection similar to the MTNG case: we consider the samples with different $\tau_{\text{sSFR}} = 9.0862, 9.2596, 9.5376$, and all galaxies, at fixed number densities. The redshifts are $z = 0.5$ (LRGs) and $z = 1$ (ELGs).

Note that in both MTNG and Astrid, AGN feedback powered by central supermassive black holes (SMBHs) is the primary quenching mechanism for massive galaxies, leading to the rising of quiescent (red) galaxy population and account for the color bimodality of galaxies in the low-redshift universe. Although the AGN

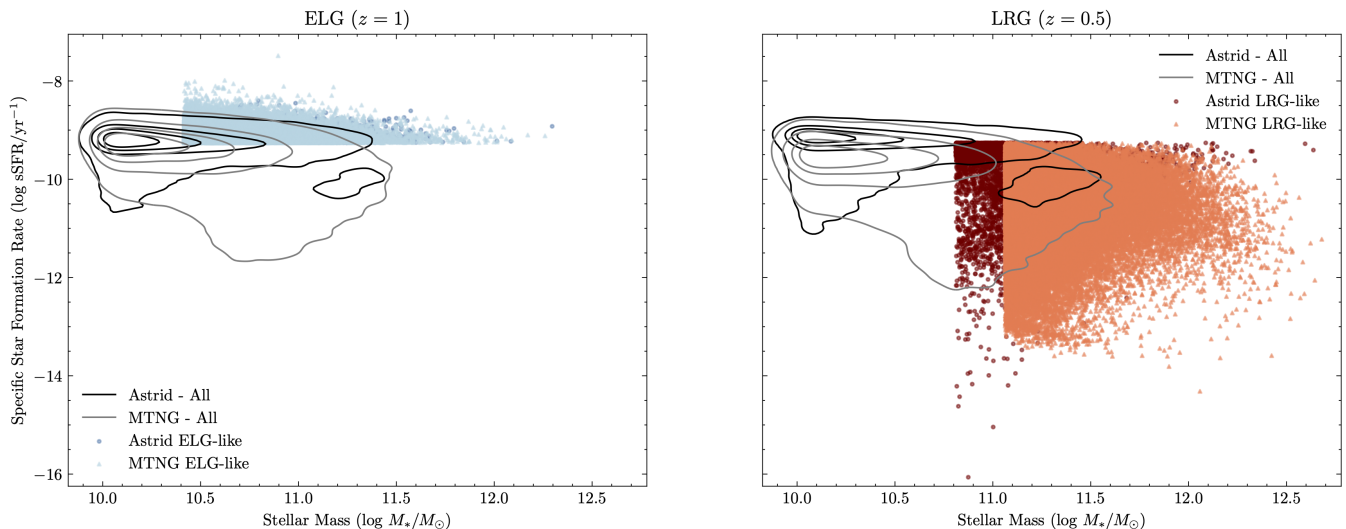


FIG. 3. The samples of MTNG and Astrid galaxies in the stellar mass - specific star formation rate planes. We display blue ELGs ($z = 1$) on the left panel and LRGs ($z = 0.5$) on the right panel. The colored distributions display the selection with the threshold $-\log(\text{sSFR}/\text{hr}^{-1}) = 9.0862$ and stellar mass cuts adjusted to reproduce the target number densities described in the main text. The black and gray contours contain 68% and 95% of all galaxies for Astrid and MTNG simulations, respectively.

feedback prescriptions in Astrid and TNG are broadly similar—employing both thermal and kinetic feedback to mimic the quasar and jet modes of AGN activity—Astrid’s AGN feedback is comparatively milder.⁴ Specifically, the jet-mode AGN feedback (which can efficiently quench galaxies) in Astrid activates only for more massive black holes ($M_{\text{BH}} \gtrsim 5 \times 10^8 M_{\odot}$), whereas in MTNG, this mode turns on at $M_{\text{BH}} \gtrsim 1 \times 10^8 M_{\odot}$. Consequently, massive galaxies ($M_{*} \gtrsim 10^{11} M_{\odot}$) in MTNG tend to have lower sSFR than those in Astrid, as seen in the galaxy selection plot in fig. 3. Most MTNG massive galaxies are strongly quenched with very low SFRs, making the LRG selection in MTNG relatively insensitive to the applied sSFR thresholds. In Astrid, many massive galaxies have sSFR values close to the threshold, making the LRG selection quite sensitive to the applied threshold.

The same argument predicts a difference in clustering properties of ELGs. Since Astrid galaxies are more star forming, we expect to find a larger abundance of ELGs at $z = 1$, and hence generically they should be less biased

than MTNG ELGs for the same sSFR threshold. Both MTNG’s and Astrid’s densities of ELG samples seen in fig. 3 have a strong response to sSFR, but the MTNG response is more monotonous within the sSFR cuts considered here. We will confirm both of these predictions at the level of the EFT parameters.

3.3. Halo occupation models

One of the goals of our study is to test how well the MTNG and Astrid galaxies can be described with the phenomenological HOD models. To that end we will compare EFT parameters of hydro galaxies with those of the HOD models. Let us describe now the HOD models and priors that we use.

Following [35, 36], all HOD samples are produced with the the `AbacusSummit small` (covariance) suite [107], with box size length $500 h^{-1} \text{Mpc}$, identical to that of MTNG.

Our comparison will be based on three halo-based galaxy samples. For LRGs, we consider two decorated models: with and without the assembly bias based on the halo concentration [12]. For ELGs, we consider the HMQ model plus additional assembly bias parameters that capture the dependence on both the local overdensity and the halo concentration. The LRG catalogs we

⁴ See [106] for a comparison of TNG and Astrid baryonic feedbacks in the context of the weak lensing surveys. Note that from the weak lensing perspective both TNG and Astrid are characterized by relatively weak feedback.

use were generated before in [35, 36]. The HMQ-based catalogs for ELGs are generated here for the first time.

For the LRGs we start with the “standard” HOD model in which the mean HOD of centrals and satellites are given by [11]

$$\begin{aligned} \langle N_c \rangle(M) &= \frac{1}{2} \left[1 + \text{Erf} \left(\frac{\log M - \log M_{\text{cut}}}{\sqrt{2}\sigma} \right) \right], \\ \langle N_s \rangle(M) &= \langle N_c \rangle(M) \left(\frac{M - \kappa M_{\text{cut}}}{M_1} \right)^\alpha, \end{aligned} \quad (1)$$

where $\text{Erf}(x)$ stands for the Gauss error function, M_{cut} , M_1 , κM_{cut} , and α are free HOD parameters. To include assembly bias, we promote M_{cut} and M_1 to be functions of the halo concentration c and the local overdensity δ , which we rank within halo mass bins and normalize the ranks to the range $[0, 1]$,

$$\begin{aligned} \log_{10} M_{\text{cut}} &\rightarrow \log_{10} M_{\text{cut}} \\ &+ A_{\text{cent}}(c^{\text{rank}} - 0.5) + B_{\text{cent}}(\delta^{\text{rank}} - 0.5) \\ \log_{10} M_1 &\rightarrow \log_{10} M_1 \\ &+ A_{\text{sat}}(c^{\text{rank}} - 0.5) + B_{\text{sat}}(\delta^{\text{rank}} - 0.5). \end{aligned} \quad (2)$$

The concentration is given by $c = r_{90}/r_{25}$, where r_f denotes the radius enclosing a fraction f of the total halo mass. The local overdensity is defined as

$$\delta = \frac{M(r_{98} < r < r_c)}{\langle M(r_{98} < r < r_c) \rangle} - 1, \quad (3)$$

where $M(r)$ is the enclosed mass of the neighbouring halos and $r_c = 5 h^{-1} \text{Mpc}$.

In addition to the above HOD implementation, we consider a satellite radial distance parameter s which is motivated by the baryonic feedback [66]. To implement it, we rank all particles inside a halo by their radial distance from the halo center, and then assign each particle a rank-dependent weight. The probability for the i -th ranked particle to host a satellite galaxy is given by

$$p_i = \frac{\langle N_s \rangle(M)}{N_P} \left(1 + s \left(1 - \frac{2r_i}{N_P - 1} \right) \right), \quad (4)$$

where N_P denotes the number of particles in a halo and r_i is the rank of particle $i \in \{0, \dots, N_P - 1\}$.

By default the velocity of the central galaxy is equal to the bulk velocity of the largest subhalo. The velocities of satellite galaxies are matched to the velocities of their host dark matter particles in the simulations. Following [17, 108], we also include velocity bias. This is done in two steps. To that end we scatter the line-of-sight

projection of the central galaxies’ velocity with random Gaussian fluctuations δv whose variance is given by the velocity dispersion of dark matter particles in a given halo σ_v . This fluctuation is additionally rescaled by the velocity bias parameter α_c :

$$v_{\text{cen},z} = v_{L2,z} + \alpha_c \delta v(\sigma_v), \quad (5)$$

where $v_{L2,z}$ is the line-of-sight projection of the subhalo velocity. As for the satellites, their velocity bias shifts them w.r.t the host particle velocity v_p as

$$v_{\text{sat},z} = v_{L2,z} + \alpha_s (v_{p,z} - v_{L2,z}), \quad (6)$$

where α_s is the satellite velocity bias. In the absence of the satellite velocity bias $\alpha_s = 1$ and hence $v_{\text{sat},z} = v_{p,z}$.

The first sample of LRG HOD models we consider was discussed in [35]. It is generated for the following set of HOD parameters drawn from uniform priors defined in [109] (here and in what follows the halo mass units are $h^{-1} M_\odot$):

$$\begin{aligned} \log_{10} M_{\text{cut}} &\in [12.4, 13.3], \quad \log_{10} M_1 \in [13.2, 14.4], \\ \log_{10} \sigma &\in [-3.0, 0.0], \quad \alpha \in [0.7, 1.5], \quad \kappa \in [0.0, 1.5], \\ B_{\text{cen}} &\in [-0.5, 0.5], \quad B_{\text{sat}} \in [-1.0, 1.0]. \end{aligned} \quad (7)$$

All other parameters are set to zero. This constitutes the main LRG-HOD sample used in our work.

The second set of catalogs is produced as part of [36]. It is generated from LRG HOD parameters which we randomly sample from the following flat distribution as suggested in [80]:

$$\begin{aligned} \log_{10} M_{\text{cut}} &\in [12, 14], \quad \log_{10} M_1 \in [13, 15], \\ \log \sigma &\in [-3.5, 1.0], \quad \alpha \in [0.5, 1.5], \\ \alpha_c &\in [0, 1], \quad \alpha_s \in [0, 2], \quad s \in [0, 1], \quad \kappa \in [0.0, 1.5], \\ A_{\text{cen}} &\in [-1, 1], \quad A_{\text{sat}} \in [-1, 1], \\ B_{\text{cen}} &\in [-1, 1], \quad B_{\text{sat}} \in [-1, 1]. \end{aligned} \quad (8)$$

In what follows we call this the LRG-HOD-II sample, as opposed to the LRG-HOD-I sample specified by eq. (7). The comparison between the two LRG catalogs can be used to estimate the impact of additional parameters. In addition, the RSD is consistently treated only in the second catalog. Our baseline redshift for both LRG HOD catalogs is $z = 0.5$.

Note that we use the CompaSO halo finder to generate the HOD priors [110]. In principle, the HOD priors are expected to depend on halo finding, and hence the halo finding mechanism should be treated as an extra “microscopic” parameter. The results of [36, 38], however, imply that the dependence of the EFT parameter priors (especially those capturing galaxy bias) on the halo finder is quite weak in practice.⁵ In particular, CompaSO and Rockstar [112] produce indistinguishable results for the quadratic bias parameters [36, 38]. CompaSO is very similar to Rockstar in terms of velocity information [110], and hence the distribution of redshift space EFT parameters from the two halo finders is also expected to be largely similar. Therefore, we will ignore the sensitivity to halo finding in what follows.

For the ELGs, we use the baseline HMQ model, in which the mean HOD of centrals is given by [80]

$$\langle N_c \rangle = 2A\phi(M)\Phi(\gamma M) + \frac{1}{2Q} \left(1 + \text{Erf} \left(\frac{\log(M/M_{\text{cut}})}{0.01} \right) \right), \quad (9)$$

where we set the quenching efficiency to $Q = 100$ following [113] and other functions are defined as

$$\begin{aligned} \phi(x) &= \mathcal{N}(\log M_{\text{cut}}, \sigma_M), \\ \Phi(x) &= \frac{1}{2} \left[1 + \text{Erf} \left(\frac{x}{\sqrt{2}} \right) \right], \\ A &= \frac{p_{\text{max}-1/Q}}{\max[2\phi(x)\Phi(\gamma x)]}. \end{aligned} \quad (10)$$

For the satellites, we use the same power-law HOD as for LRGs, eq. (1). In addition, we include assembly bias and velocity bias using the same approach as for LRGs, i.e. eqs. (2). We sample the HMQ parameters from the following uniform distributions:

$$\begin{aligned} \log M_{\text{cut}} &\in [11.6, 12.6], & \log M_1 &\in [12.5, 18], \\ \log \sigma &\in [-3.5, 1.0], & \alpha &\in [0, 1.2], \\ \alpha_c &\in [0, 1], & \alpha_s &\in [0, 2], & s &\in [-1, 1], & \kappa &\in [0, 10], \\ p_{\text{max}} &\in [0.05, 1], & \gamma &\in [1, 15] \\ A_{\text{cen}} &\in [-1, 1], & A_{\text{sat}} &\in [-1, 1], \\ B_{\text{cen}} &\in [-1, 1], & B_{\text{sat}} &\in [-1, 1]. \end{aligned} \quad (11)$$

⁵ The discrepancy between the friends-of-friends (FoF) [111] and Rockstar methods is quite significant at the level of the redshift-space counterterms. However, the standard FoF does not consistently incorporate velocity information, and hence Rockstar is expected to provide more accurate results.

We do not vary Q following [80], but in principle one can easily sample this parameter too.

We generate 10500 catalogs of ELG-type galaxies based on the `AbacusSummit small` suite. Our baseline redshift for ELGs is $z = 1.1$. To obtain the EFT parameters, we fit the synthetic galaxy density maps in redshift space with the field-level EFT forward model of [35, 36, 43, 49, 51]. Our approach is identical to the one used in [35, 36]. The details of the field-level forward model are given below.

3.4. Field level EFT

Our EFT parameter fits are based on the field-level forward model introduced in refs. [43, 49]. Its key elements are various shifted operators in the bias expansion. The shifted operators are defined as

$$\tilde{\mathcal{O}}(\mathbf{k}) = \int d^3\mathbf{q} \mathcal{O}(\mathbf{q}) e^{-i\mathbf{k}\cdot(\mathbf{q} + \boldsymbol{\psi}_1(\mathbf{q}) + f\hat{z}(\boldsymbol{\psi}(\mathbf{q})\cdot\hat{z}))}, \quad (12)$$

where \mathbf{q} is the Lagrangian coordinate, $\mathcal{O}(\mathbf{q})$ is an operator in Lagrangian space, $\boldsymbol{\psi}_1$ is the Zel’dovich displacement,

$$\boldsymbol{\psi}_1(\mathbf{q}, z) = \int d^3q e^{i\mathbf{q}\mathbf{k}} \frac{i\mathbf{k}}{k^2} \delta_1(\mathbf{k}, z), \quad (13)$$

and f is the logarithmic growth rate. δ_1 above is the linear matter density field, which obeys the Gaussian statistic:

$$\langle \delta_1(\mathbf{k}) \delta_1(\mathbf{k}') \rangle = (2\pi)^3 \delta_D^{(3)}(\mathbf{k}' + \mathbf{k}) P_{11}(k). \quad (14)$$

In what follows we will use primes to denote stripping off the Dirac delta function,

$$\langle \delta_1(\mathbf{k}) \delta_1(\mathbf{k}') \rangle' = P_{11}(k). \quad (15)$$

For real space (rest-frame) observables we set $f = 0$ in eq. (12). To avoid operator mixing, the shifted operators are orthogonalized as

$$\langle \tilde{\mathcal{O}}_m^\perp \tilde{\mathcal{O}}_n^\perp \rangle = 0 \quad \text{if } n \neq m. \quad (16)$$

The EFT forward model in redshift space is given by

$$\begin{aligned} \delta_g^{\text{EFT}}(\mathbf{k}, \hat{z}) &= \delta_Z(\mathbf{k}, \hat{z}) - \frac{3}{7} \mu^2 f \tilde{\mathcal{G}}_2 \\ &+ \beta_1(k, \mu) \tilde{\delta}_1(\mathbf{k}, \hat{z}) + \beta_2(k, \mu) (\tilde{\delta}_1^\perp)^\perp(\mathbf{k}, \hat{z}) \\ &+ \beta_{\mathcal{G}_2}(k, \mu) \tilde{\mathcal{G}}_2^\perp(\mathbf{k}, \hat{z}) + \beta_3(k, \mu) (\tilde{\delta}_1^\perp)^\perp(\mathbf{k}, \hat{z}), \end{aligned} \quad (17)$$

where

$$\mu = (\mathbf{k} \cdot \hat{z})/k. \quad (18)$$

The different bias operators are defined as follows. \mathcal{G}_2 is the tidal operator with the unsymmetrized kernel

$$\mathcal{G}_2(\mathbf{k}) = \int_{\mathbf{p}} F_{\mathcal{G}_2}(\mathbf{p}, \mathbf{k} - \mathbf{p}) \delta_1(\mathbf{p}) \delta_1(\mathbf{k} - \mathbf{p}), \quad (19)$$

$$F_{\mathcal{G}_2}(\mathbf{k}_1, \mathbf{k}_2) = \frac{(\mathbf{k}_1 \cdot \mathbf{k}_2)^2}{k_1^2 k_2^2} - 1,$$

$\int_{\mathbf{k}} \equiv \int \frac{d^3 \mathbf{k}}{(2\pi)^3}$ and Γ_3 is the Galileon tidal operator,

$$F_{\Gamma_3} = \frac{4}{7} \left(1 - \frac{(\mathbf{k}_1 \cdot \mathbf{k}_2)^2}{k_1^2 k_2^2} \right) \left(\frac{((\mathbf{k}_1 + \mathbf{k}_2) \cdot \mathbf{k}_3)^2}{(\mathbf{k}_1 + \mathbf{k}_2)^2 k_3^2} - 1 \right). \quad (20)$$

The above kernel should be used in conjunction with the appropriate Fourier transform. For a general cubic operator $\mathcal{O}^{(3)}$ we use the definition

$$\mathcal{O}^{(3)} = \int_{\mathbf{k}_1} \int_{\mathbf{k}_2} \int_{\mathbf{k}_3} \left(\prod_{i=1}^3 \delta_1(\mathbf{k}_i) \right) (2\pi)^3 \delta_D^{(3)}(\mathbf{k} - \mathbf{k}_{123}) F_{\mathcal{O}^{(3)}}. \quad (21)$$

The transfer functions are then measured from the simulated density field snapshots δ^{truth} :

$$\beta_i(k) = \frac{\langle \mathcal{O}_{i}^{*\perp}(\mathbf{k}) \delta_g^{\text{truth}}(\mathbf{k}) \rangle'}{\langle |\mathcal{O}_{i}^{\perp}(\mathbf{k})|^2 \rangle}. \quad (22)$$

The real space forward model is obtained by setting $f = 0$ in (17) and removing the Zel'dovich field δ_Z (whose contribution is degenerate with $\beta_1 \tilde{\delta}_1$). The transfer functions in this case do not depend on the line-of-sight.

Due to the presence of the stochastic components, the forward model always has noise, whose power spectrum is given by

$$P_{\text{err}}(k, \mu) = \langle |\delta^{\text{EFT}}(\mathbf{k}, \hat{\mathbf{z}}) - \delta^{\text{truth}}(\mathbf{k}, \hat{\mathbf{z}})|^2 \rangle' \quad (23)$$

In EFT, the theoretical prediction for the error power spectrum is given by

$$P_{\text{err}}(k, \mu) = \frac{1}{\bar{n}} \left(1 + \alpha_0 + \alpha_1 \left(\frac{k}{k_S} \right)^2 + \alpha_2 \mu^2 \left(\frac{k}{k_S} \right)^2 \right), \quad (24)$$

where we have omitted higher derivative contributions. We choose $k_S = 0.45 \text{ hMpc}^{-1}$ following [28].

The bias parameters and counterterms are extracted by fitting the transfer functions and the error spectra with the EFT predictions using the methodology of ref. [36] based on time-sliced perturbation theory [22, 23]. We use $k_{\text{max}} = 0.4 \text{ hMpc}^{-1}$ and $k_{\text{max}} = 0.2 \text{ hMpc}^{-1}$ for real and redshift space transfer function fits, respectively. We apply the same scale cuts to the noise power spectra.

For Astrid the residual sample variance is very large at $k_{\text{max}} = 0.2 \text{ hMpc}^{-1}$, so we use $k_{\text{max}} = 0.4 \text{ hMpc}^{-1}$ both in real and redshift spaces.

4. HYDRODYNAMIC GALAXIES IN THE FIELD LEVEL EFT

Let us discuss now the results of our field-level measurements from the hydrodynamic simulations.

4.1. MTNG results

The density fields and transfer functions extracted from MTNG are shown in fig. 4 and fig. 5. Visually, these transfer functions are very similar to those measured by us from HOD mocks [35]. An important parameter is the error power spectrum P_{err} (see eq. (23)) as a function of k , which is related to the cross-correlation coefficient, $r_{cc}^2 = 1 - P_{\text{err}}/P_{\text{truth}}$, shown in fig. 6 for DESI-like LRGs and ELGs. First, we see that the error power spectrum is approximately scale-independent, in perfect agreement with the EFT predictions. Second, from fig. 6 we see that the cross-correlation coefficient is quite large for wavenumbers $k \lesssim 0.4 \text{ hMpc}^{-1}$, implying that EFT correctly reproduces the entire density field on quasi-linear scales. The cross-correlation coefficient is larger for the LRG sample because they have a larger bias at the same number density as ELGs. Third, we see that the scale-dependence of P_{err} becomes sizeable only around $k \simeq 0.5 \text{ hMpc}^{-1}$, just like in the HOD samples from [35]. This suggests that the EFT model for the hydrodynamical galaxies has a similar momentum reach k_{max} as the HOD-based mocks. This is further confirmed by direct fits to the transfer functions, which we use to extract the EFT parameters.

For DESI-like galaxies, the real space EFT parameters, including galaxy bias parameters, are depicted by dots in fig. 1, while the redshift space counterterms are shown in fig. 7. In the background of this figure, we show measurements from the HOD-based mocks (HOD-LRG-I) from ref. [35] for bias parameters and ref. [36] for redshift space counterterms. We display the measurements for BOSS-like galaxies in fig. 8. In addition, we show the priors from the extended LRG-HOD-II sample. Different selections in this figure are referred to as $\text{sSFR}_{\tau_{\text{SFR}}}$, e.g. $\text{sSFR}_{9.0862}$ etc. LRGs/ELGs have larger/smaller

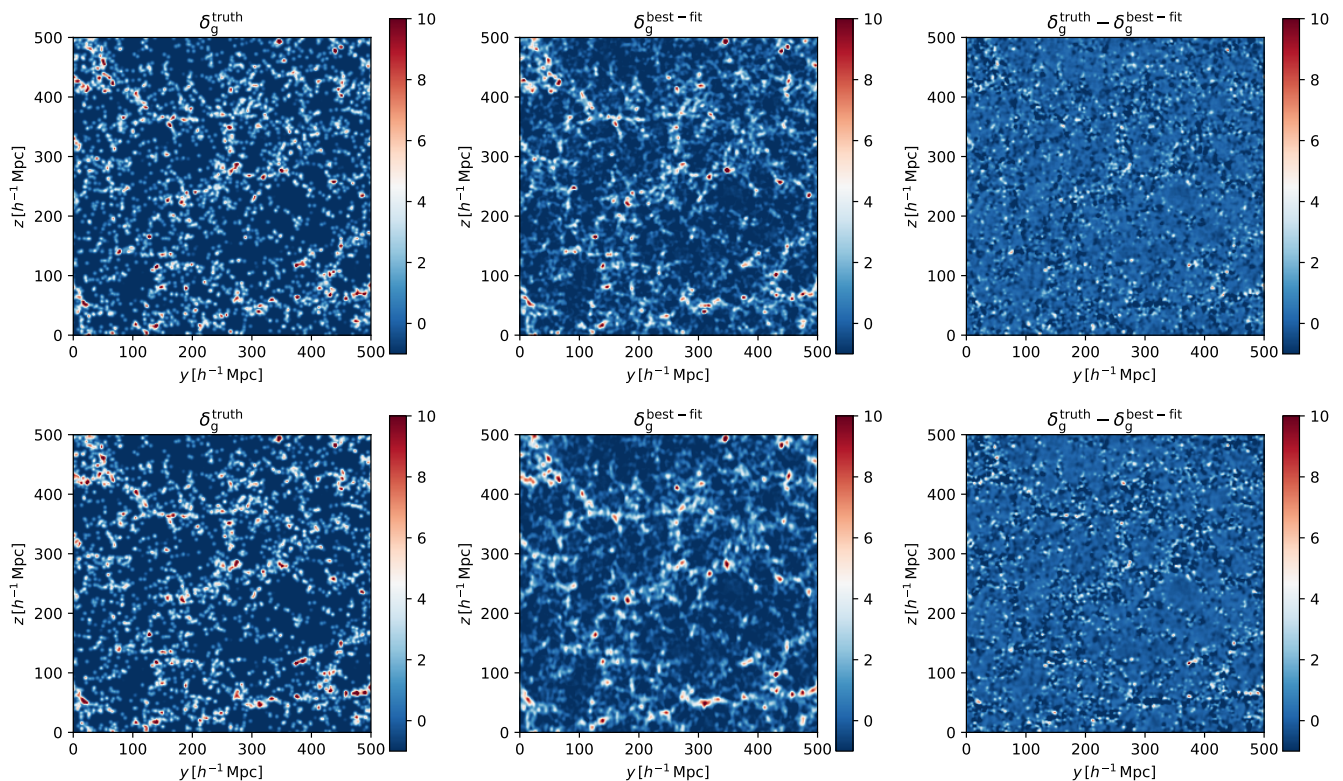


FIG. 4. The MTNG DESI-like LRG density field in real space (upper panel) and in redshift space (lower panel) from the MTNG simulation (left), its best field-level EFT fit (center), and the residuals between the two (right). The square of the rightmost field gives the error power spectrum. For visualization purposes, the field has been smoothed with a $R = 2 h^{-1} \text{Mpc}$ 3D Gaussian filter. The depth of each panel is $\approx 60 h^{-1} \text{Mpc}$. The redshift space distortions are applied along the z -axis.

τ_{SFR} than the thresholds, respectively. We see that all the LRG data points are fully consistent with the HOD-based priors from the LRG-HOD-II sample.

Let us discuss LRG datapoints first. We see that in general these are very consistent with the HOD-based values. For most of the parameters, the MTNG measurements lie within the 68% probability density area. The only parameter that is systematically outside of the 68% confidence interval is the sub Poisson stochasticity α_0 , which still lies within the 95% CL. Let us note that variations of the specific star formation rate do not significantly change the values of LRG bias parameters. This is consistent with the previous studies of the b_2 and b_1 parameters from IllustrisTNG [57], which considered a much wider variation of sSFR than us. The agreement between MTNG and TNG on the sSFR-dependence of b_1 and b_2 implies that the weak response of MTNG LRGs to sSFR is a genuine property of the TNG feedback. This point will be discussed further in comparison with Astrid galaxies. Comparing DESI and BOSS-like LRGs, we see

that the only relevant parameter that changes the values of EFT parameters in MTNG is the number density.

We emphasize that our comparison so far has been based on the LRG-HOD-I sample of [35], which does not include the concentration-dependent assembly bias parameters $A_{\text{cent}}, A_{\text{sat}}$. Although these parameters can be included in HOD samples as in [36], we see that they are not necessary in order to reproduce EFT parameters from MTNG.

Let us now move on to the redshift space counterterms, see fig. 7. Overall, we see great consistency here as well: all MTNG parameters lie within 95% CL of the HOD-based parameter densities. Curiously, we notice a small spread of counterterm values due to variations of sSFR, but it does not exceed the residual statistical error associated with sample variance, and hence it cannot be robustly interpreted as a genuine response to sSFR. We also note that the MTNG LRGs exhibit somewhat weaker fingers-of-God than the HOD galaxies, and than the actual BOSS samples [25, 56].

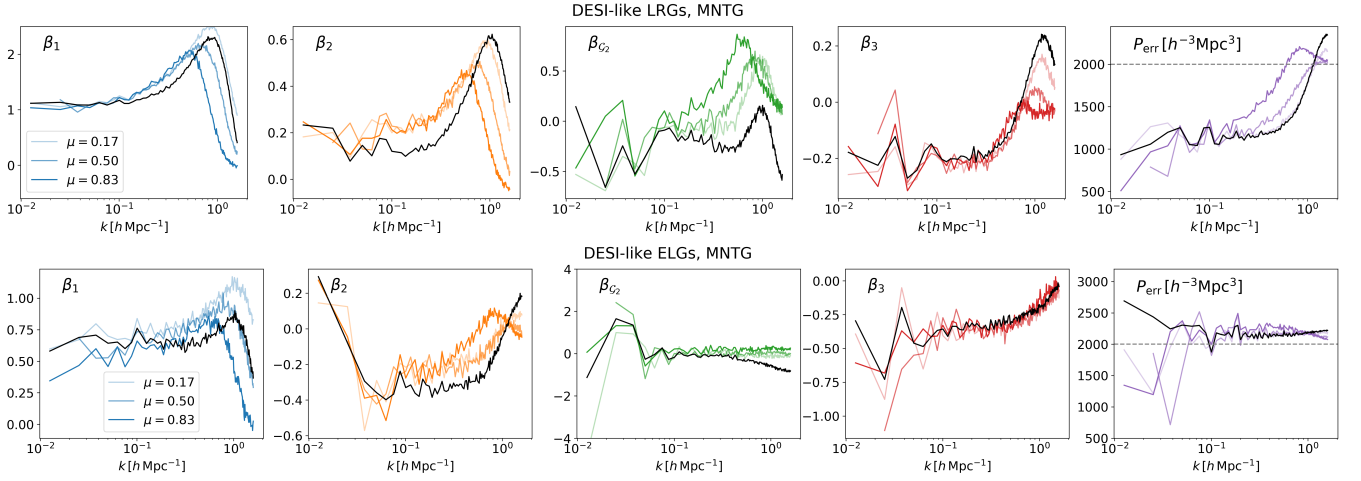


FIG. 5. EFT model transfer functions and noise power spectra for MTNG galaxies in real space (black lines) and in redshift space, for three μ bins. Note that we subtract 1 and 0.5 from the real space transfer functions for β_1 and β_{G_2} to match the low- k limit of the redshift space transfer functions. The dashed line in the rightmost panel depicts the \bar{n}^{-1} Poisson prediction.

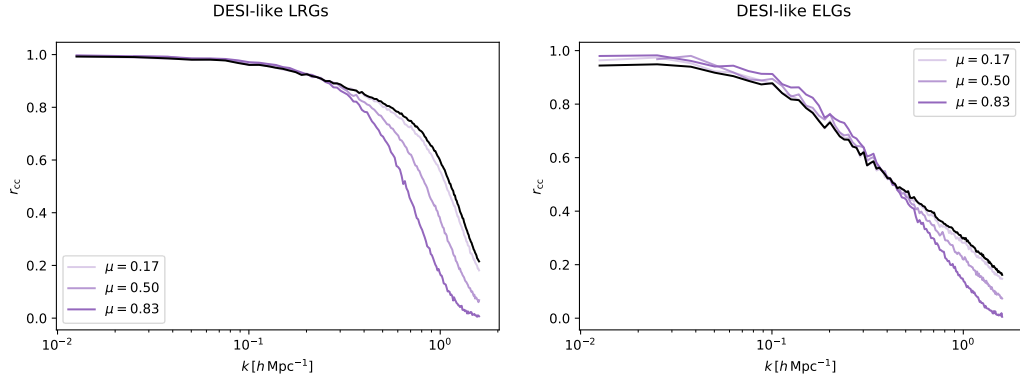


FIG. 6. Cross-correlation coefficients r_{cc} between the MTNG LRGs (left panel) and ELGs (right panel). r_{cc} measures the accuracy of the EFT model. For $k \lesssim 0.1 h\text{Mpc}^{-1}$ it is closer to unity, implying that the galaxy distribution is almost entirely correlated with the EFT operators built out of dark matter density and tidal fields. On large scales, the line-of-sight modes (non-zero μ) increase the correlation with dark matter thanks to the linear Kaiser effect. The enhancement is proportional to f/b_1 , which is larger for ELGs, owing to the higher redshift and smaller b_1 .

Finally, let us discuss MTNG ELGs, whose bias parameters are shown in both fig. 1 and fig. 2. Looking at fig. 1, we see that their bias parameters exhibit a significant discrepancy with the HOD-LRG priors: the ELG data point lies outside of the HOD based density in the $b_2 - b_1$, $b_1 - b_2$ and $b_2 - b_3$ planes. For all other real space parameters the agreement is quite good. We have checked that considering a wider range of values for HOD parameters and including additional assembly bias parameters as in the LRG-HOD-II sample [36] does not allow one to widen the density of the local bias parameter towards the ELG values. We will see shortly that

the tension is driven by the specific form of the HOD for ELGs which is not captured by the HOD model used in [35, 36] aimed at reproducing LRG clustering. This is confirmed in fig. 2, where we plot our MTNG ELG measurements on top of the EFT parameters following from the HMQ models.

As for the redshift space ELG parameters, we see that the MTNG values are significantly smaller than those of LRG-HODs. They are also typically smaller than the LRG redshift space counterterms from MTNG. This suggests that ELGs may exhibit significantly weaker fingers-of-God than LRGs in general. This is confirmed at the

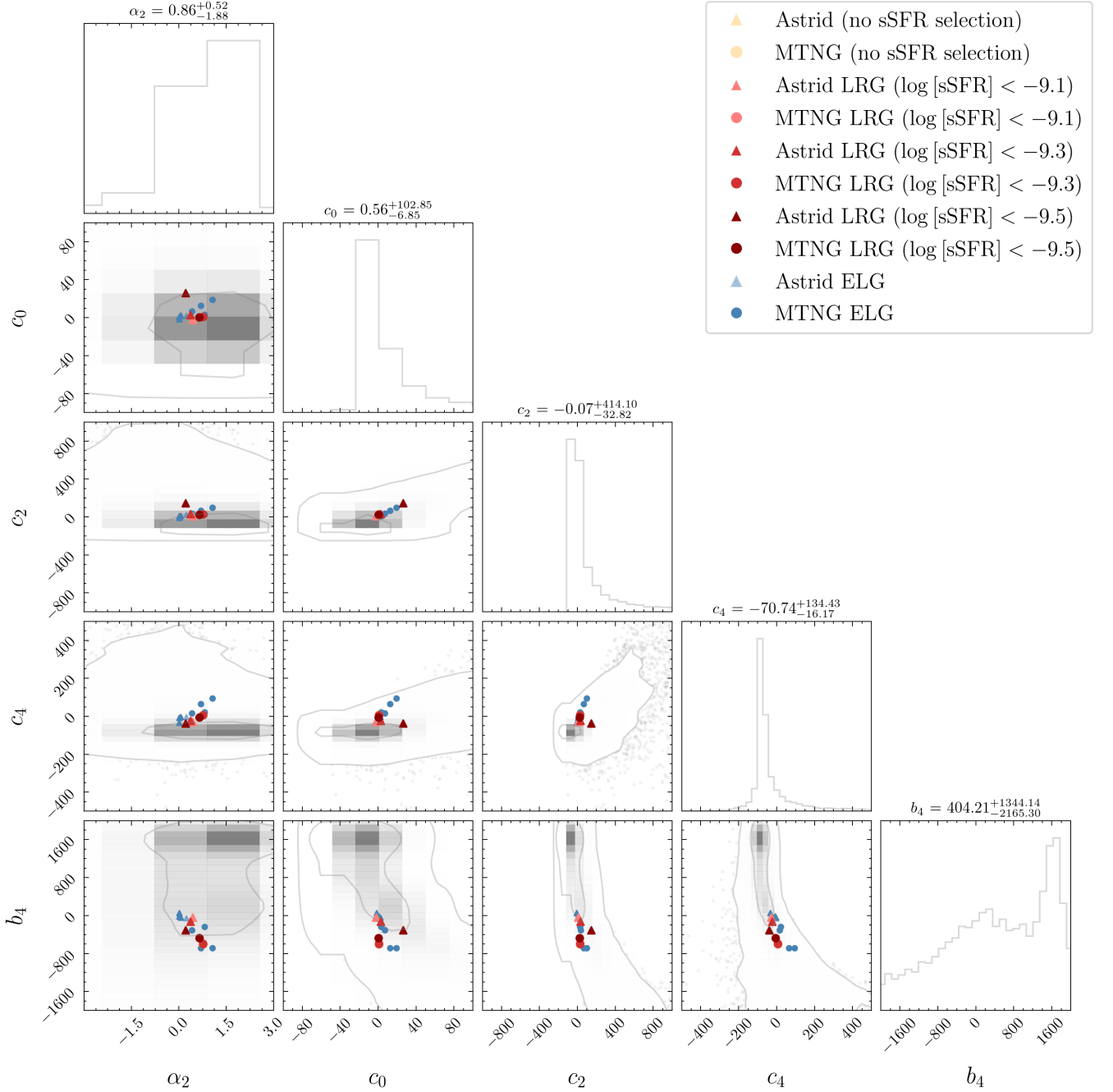


FIG. 7. MTNG and Astrid redshift-space counterterms for LRGs and ELGs vs the LRG-HOD priors.

level of our HMQ-based priors, see fig. 10. There, we observe that the distribution of the counterterms from HMQ is much narrower than that of the LRG-based HODs.

Let us also note that there is an apparent $\sim 2\sigma$ tension between the MTNG and HMQ-based counterterm values in the $\alpha_2 - b_4$ and $\alpha_2 - c_4$ planes. While this tension is not significant, it will be still interesting to understand its origin.

4.2. Astrid results

The Astrid EFT transfer functions are shown in fig. 9. As in the MTNG case, they look very similar to those of HOD-LRGs from ref. [36].

Comparing the LRG datapoints in fig. 1, one may notice that in contrast to MTNG, the sSFR cuts have a significant effect on the Astrid galaxies. In addition, al-

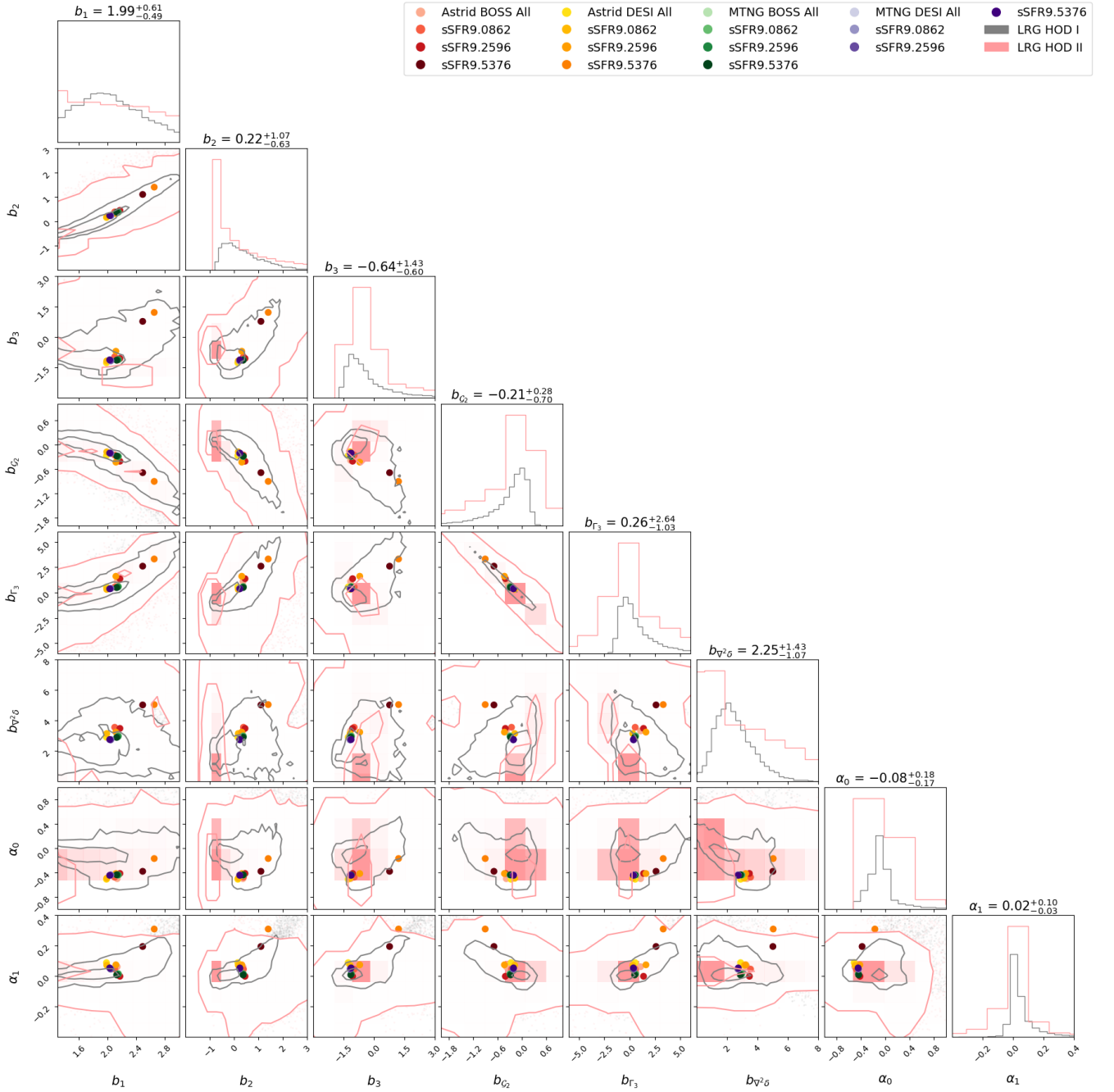


FIG. 8. MTNG and Astrid real space EFT parameters of LRGs against two LRG-HOD-based distributions: LRG-HOD-I (gray) and LRG-HOD-II (pink). In contrast to LRG-HOD-I, LRG-HOD-II priors include concentration-dependent HODs and have wider priors on the other HOD parameters.

though most of the datapoints still lie within 95% CL, we see clear outliers for many EFT parameters. For instance, we see some noticeable outliers only in the $b_{\nabla^2\delta}$ and α_1 planes. For $b_{\nabla^2\delta}$, the deviations are quite natural as the HOD mocks e.g. do not fully account for the baryonic feedback, which is captured in hydrodynamic

simulations. We note however, that the tension w.r.t. the HOD values of $b_{\nabla^2\delta}$ is not very significant. In particular, the $b_{\nabla^2\delta}$ distribution from HOD becomes noticeably wider once wider HOD-LRG-II priors are considered, as in fig. 8, in which case we find perfect agreement with Astrid.

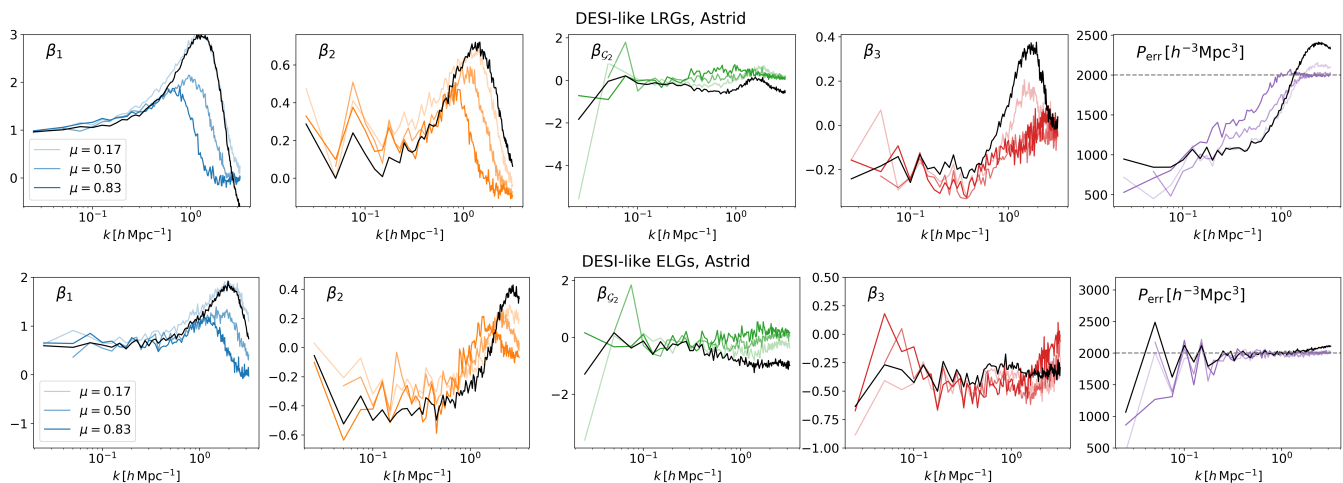


FIG. 9. Same as fig. 5 but for the Astrid simulation.

The different response of MTNG and Astrid galaxies to sSFR cuts can be understood from the arguments given in Sec. 3.2 and from fig. 3: Astrid LRGs have a stronger dependence on sSFR than MTNG ones. While the distribution of LRGs is approximately constant as a function of sSFR for low sSFR values for both Astrid and MTNG, the Astrid distribution changes dramatically as one lowers the sSFR (increases τ_{sSFR}). The MTNG distribution, however, remains approximately constant in the interval $\log(\text{sSFR}/\text{yr}^{-1}) \in [-11, -9]$. In other words, most of the LRG samples are concentrated far from the selection threshold for low τ_{sSFR} , but then their density changes differently when lowering τ_{sSFR} , in agreement with expected differences in the feedback assumptions. This picture is consistent with the phenomenology seen in fig. 1: LRGs' biases for galaxies with a low star formation rate from MTNG and Astrid are quite similar, and their response to sSFR is quite modest. However, the discrepancy between MTNG and Astrid grows with τ_{sSFR} . Larger τ_{sSFR} in Astrid corresponds to more massive, more biased halos, which explains why $b_{\nabla^2\delta}$ values are large for these samples.

One may also notice some $\simeq 2\sigma$ outliers in the b_{Γ_3} and α_1 planes, which suggest that spatial non-localities are quite significant for Astrid galaxies. The data points from Astrid exhibit a mild tension with HOD model considered in [35], and their reproduction within these models may require fine-tuned HOD parameters. However, once we consider extended decorated LRG-HOD models from the LRG-HOD-II sample in fig. 8, all LRG data points become highly consistent with them. Together

with the $b_{\nabla^2\delta}$ behavior, this suggests that an extended set of HOD parameters as in [36] may be needed in order to capture the higher derivative bias of LRGs within the HOD framework.

Let us discuss now the Astrid ELGs. As in the MTNG case, their local bias parameters b_1, b_2, b_3 exhibit significant tensions with the LRG-HOD model. Our results suggest that even in the context of the decorated HOD models there is no way to reproduce the large-scale local bias parameters of ELG galaxies. The anomalous behavior, again, is captured by the HMQ-based samples, see fig. 2.

As far as the ELGs' response to sSFR is concerned, both Astrid and MTNG galaxies have a significant response, consistent with their selection seen in fig. 3. Note however that the precise values of EFT parameters for the same sSFR cuts, and the response as a function of sSFR are slightly different between MTNG and Astrid. Astrid's ELGs are less biased than MTNG ones for the same sSFR cuts, while the MTNG response to sSFR is smoother. This, again, can be understood from fig. 3: we see that the Astrid ELGs do not response monotonically to lowering of sSFR as their distribution peaks around $\tau_{\text{sSFR}} \approx 9.3$, and hence the response to sSFR slows down around this value. In contrast, the MTNG ELG distribution plateaus only around $\tau_{\text{sSFR}} \approx 10$, growing towards this value monotonically. This explains why the Astrid results for $\tau_{\text{sSFR}} = 9.25$ and $\tau_{\text{sSFR}} = 9.54$ are almost the same, while the MTNG EFT parameters keep changing at the same pace as one raises τ_{sSFR} in this region.

In addition, before reaching the plateau, the density

of Astrid ELGs is visibly larger than that of MTNG's (which can be appreciated by comparing the black and gray contours in fig. 3). This, again, can be traced back to the fact that massive galaxies in Astrid have a larger sSFR, implying larger abundance and consequently a lower linear bias of their ELGs, consistent with our measurements.

Finally, we note that the redshift-space EFT counterterms are very consistent with those of our HOD-LRG distribution in fig. 7. The comparison against the HMQ priors is given in fig. 10. As in the MTNG case, we see that the typical amplitude of the FOG ELG counterterms is smaller than those of the HOD-LRG samples. Note that the $\log[\text{sSFR}] > -9.3$ samples correspond to galaxies with low star formation, which do not actually represent the observed ELGs. In terms of the selection used in [64], they actually correspond to LRGs, and hence, strictly speaking, one should not compare them with HMQ samples. In agreement with this argument, we see that their counterterms are actually stronger than those based on the HMQ samples. For the consistent choice of sSFR selection $\log[\text{sSFR}] > -9.1$, Astrid counterterms perfectly agree with the HMQ priors, see fig. 10. In particular, RSD counterterms for Astrid ELGs match well the mean values of the HMQ-based samples.

4.3. Quadratic bias parameters of galaxies and halos

One important result of our work is the new measurement of quadratic bias parameters from the MTNG and Astrid simulations. The quadratic bias parameters b_2 and b_{G_2} have been extensively studied in the literature, see e.g. [38–41, 55, 57, 83, 84, 114]. Let us compare our measurements of b_2 and b_{G_2} from hydro galaxies with this literature and with the values extracted from our halo occupation models.

Our main results are summarized in Fig. 11. For simplicity, we combine the Astrid and MTNG measurements. First, let us discuss the local bias parameter b_2 as a function of the linear bias parameter b_1 . The first point of comparison is the $b_2(b_1)$ function of dark matter halos. It is shown in the left panel of Fig. 11 as a numerical fit from the analysis of [84], and also as direct measurements of $b_2(b_1)$ values from the *Quijote* simulation [115] from [36]. We see that the LRG $b_2(b_1)$ curve lies sys-

tematically above the halo curve for $b \sim 2.2$, but the difference between them decreases for larger values of b_1 . This trend was first pointed out by [83]. The hydro ELG, however, agree well with the pure halo predictions. The second point of comparison is between the hydro galaxies and the HOD/HMQ-based samples. There we see a high level of consistency: both LRG and ELG from our hydro simulations match well the halo-based values.

The intricate behavior of galactic b_2 values can be easily understood as a consequence of the specific HOD shape for different galaxies. In general, the b_2^g of galaxies is given by the $b_2^h(M)$ of halos, weighted with the halo mass function and the HOD [18, 38]:

$$b_2^g = \frac{1}{\bar{n}_g} \int dM \frac{d\bar{n}_h}{dM} \langle N \rangle(M) b_2^h(M), \quad (25)$$

where $\langle N \rangle = \langle N_c \rangle + \langle N_s \rangle$ is the average HOD, \bar{n}_g is the galaxy number density, and $\frac{d\bar{n}_h}{dM}$ is the halo mass function. Let us discuss the LRG case first. Let us ignore the satellites, assume for simplicity that the HOD can be approximated as a Heaviside step function, $\langle N_c \rangle(M) \approx \Theta_H(M - M_{\text{cut}})$, and approximate $b_2^h(M)$ around its minimum as a parabola,

$$b_2^h(M) \approx -b_2^{\text{min}} + b_2' (\ln M - \ln M_0)^2,$$

with $b_2^{\text{min}}, b_2' > 0$. For the Press-Schechter halo mass function in a Planck-like cosmology $M_0 \approx 10^{12.4} h^{-1} M_\odot$ at $z = 0.5$ ($M_0(z = 1) \approx 10^{12} h^{-1} M_\odot$) [18, 116]. This implies

$$b_2^g \approx -b_2^{\text{min}} + b_2' \frac{1}{\bar{n}_g} \int_{M_{\text{cut}}} dM \frac{d\bar{n}_h}{dM} (\ln M - \ln M_0)^2. \quad (26)$$

Obviously, the rightmost term above is greater than zero, so that b_2^g will always be greater than the minimal value of b_2 of halos $-b_2^{\text{min}}$. Let us further specify now that $\frac{d\bar{n}_h}{dM} \propto M^{-n}$ for $M < M_*$, which is a good approximation for light halos in a Λ CDM universe within the Press-Schechter model (for which $n \approx 2$ and $M_* \sim 10^{14} M_\odot/h$). Then the integral in eq. (26) is dominated by its lower limit, which gives:

$$b_2^g \approx -b_2^{\text{min}} + b_2' \ln^2 x + \frac{2b_2'}{(n-1)^2} [1 + (n-1) \ln x], \quad (27)$$

with $x \equiv M_{\text{cut}}/M_0$. Comparing this with the relevant halo value,

$$b_2^h(M_{\text{cut}}) = -b_2^{\text{min}} + b_2' \ln^2 x, \quad (28)$$

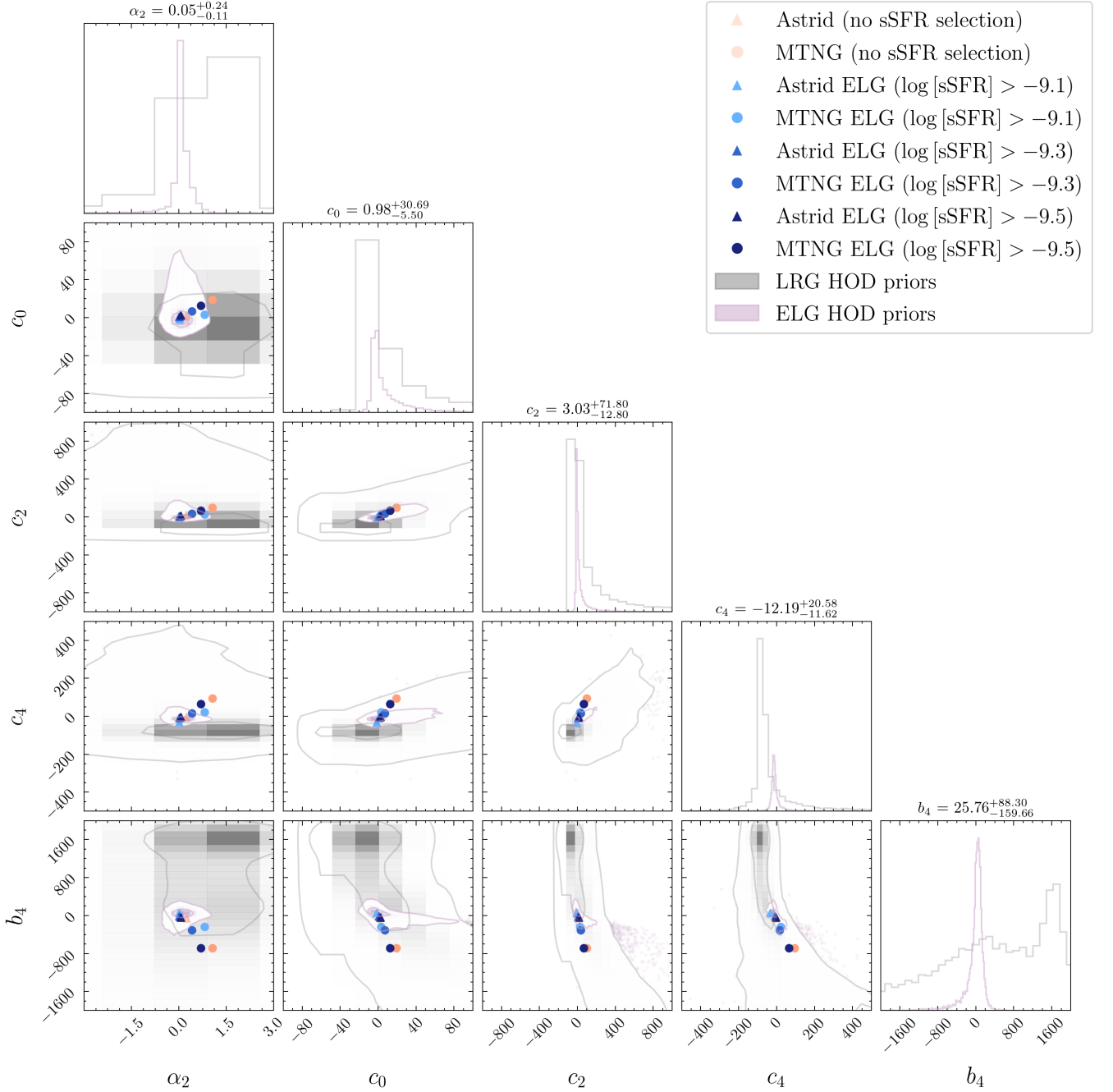


FIG. 10. MTNG and Astrid redshift-space counterterms for ELGs vs the LRG-HOD and ELG-HMQ based distributions.

and recalling that $M_{\text{cut}} \gtrsim M_0$ for our baseline LRG-HOD-I sample, we see that this formula correctly reproduces the additional enhancement of galactic b_2 :

$$\begin{aligned}
 b_2^g - b_2^h &= b_2' \frac{2}{(n-1)^2} [1 + (n-1) \ln x] \\
 &\approx 2b_2'(1 + \ln(M_{\text{cut}}/M_0)) ,
 \end{aligned}
 \tag{29}$$

In the case $M_0 \gtrsim M_{\text{cut}}$ relevant for some mocks in our extended HOD-LRG-II sample, we still have an enhance-

ment, albeit somewhat smaller, because the logarithm in the r.h.s. above is negative but bounded from below, $\ln(M_0/M_{\text{cut}}) > -1$.

Note that our derivation above is very simplistic, yet it shows that key to understanding the LRGs' b_2 is the shape of their HOD, plus the fact that these galaxies typically reside in halos whose masses are larger than M_0 that minimizes $b_2^h(M)$. We have ignored the satellites in our

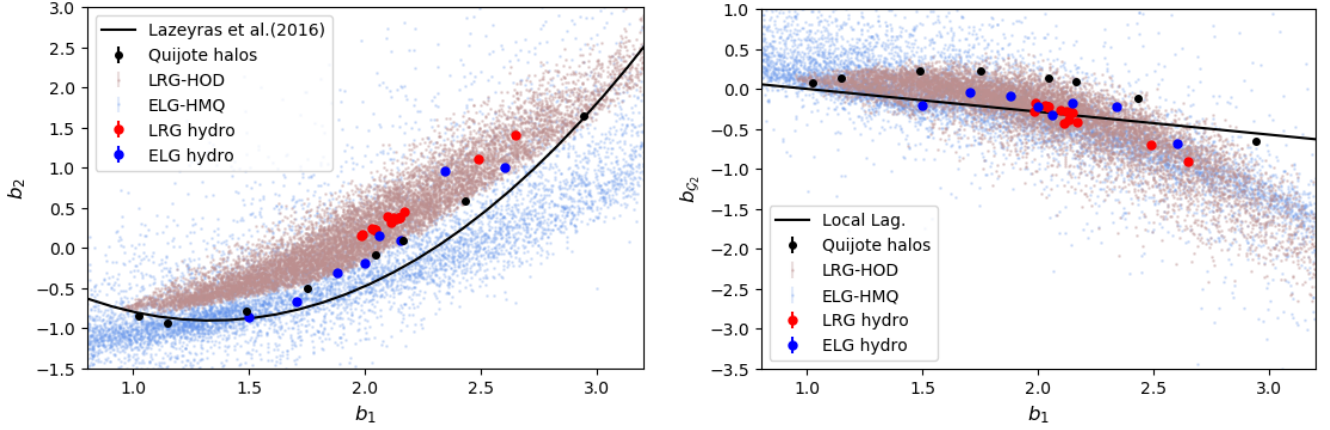


FIG. 11. Quadratic bias parameters b_2 and b_{G_2} as functions of b_1 from the Quijote halos, LRG-HOD mocks, ELG-HQM mocks, and the hydro simulations MTNG and Astrid. The black curve represents the fit for $b_2(b_1)$ of halos from [84] (left panel), and the prediction of the local Lagrangian model for b_{G_2} (right panel).

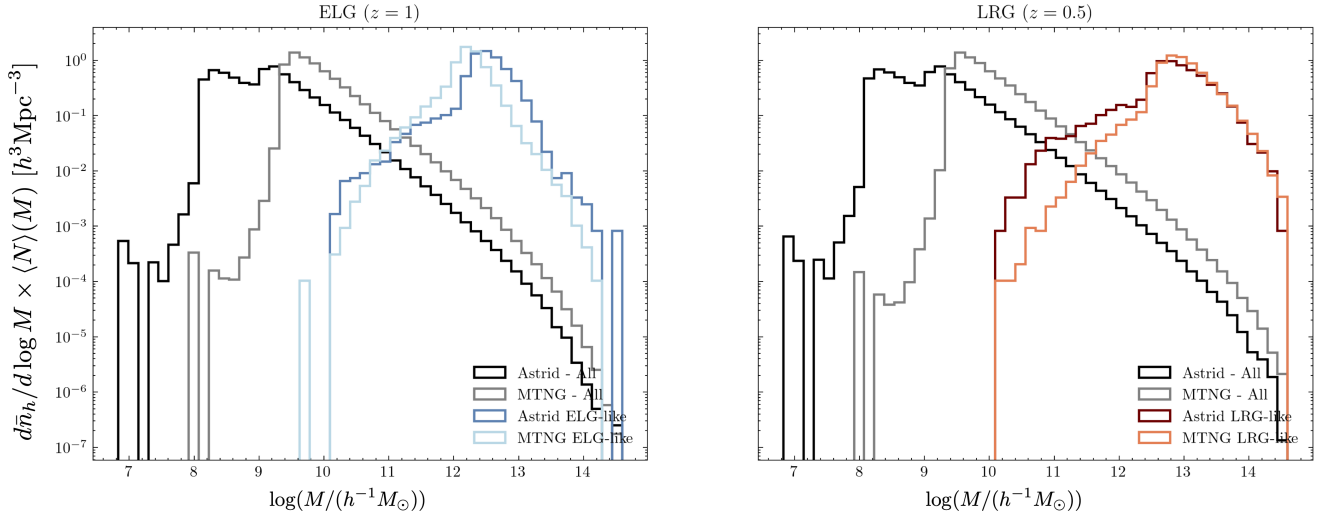


FIG. 12. The mass function of halos hosting the hydrodynamic galaxies, i.e. $\frac{d\bar{n}_h}{d\log M} \langle N \rangle (M)$ where $\langle N \rangle (M)$ is the halo occupation distribution. The selection of galaxies matches the one displayed in fig. 3.

discussion, but their growing with mass HOD shape will always additionally enhance the total b_2 of the sample.

The total effective weight of the galaxy bias $\frac{d\bar{n}_h}{dM} \langle N \rangle$ that appears in the EFT parameter relations such as eq. (25) is quite broad for $M > M_0$, see Fig. 12 that displays the mass function of halos hosting the Astrid and MTNG galaxies. In Fig. 12 the weight peaks at $M \sim 10^{13} h^{-1} M_\odot$ and then extends towards larger masses. This implies that the HOD weighting always produces a positive correction to b_2 , which explains the observed enhancement.

As far as the ELG are concerned, their HOD weighted

by the halo mass function has a narrow peak (around $M \sim 10^{12} h^{-1} M_\odot$ in fig. 12), which can be crudely approximated as a Dirac delta-function, $\langle N \rangle \frac{d\bar{n}_h}{dM} \propto \delta_D(M - M_{\text{cut}})$. In this case we obviously reproduce the desired leading order result $b_2^g(M_{\text{cut}}) \approx b_2^h(M_{\text{cut}})$. Going beyond the delta-function limit, we can see that the size of the correction to b_2 is determined by the spread of the HOD bias weighting function $\frac{d\bar{n}_h}{dM} \langle N \rangle$. This, in addition with the ELGs populating lighter halos, results in the spread of the b_2 values around the halo curve for ELG which can be observed in Fig. 11. Thanks to the ELG HOD weight, the fluctuations around the halo values can be

both positive and negative, as can be seen in fig. 11.

Let us now discuss the tidal bias $b_{\mathcal{G}_2}$ as a function of b_1 , shown in the right panel of Fig. 11. The first point of comparison is the dark matter halo values from **Quijote**. We see that in general the galaxy $b_{\mathcal{G}_2}$ values lie below the halo values. The second point of comparison is with the local Lagrangian prediction $b_{\mathcal{G}_2}^{\text{Local Lag.}} = -(2/7)(b_1 - 1)$. There, we see that $b_{\mathcal{G}_2}$ of our hydro galaxies indeed matches well the local Lagrangian model for $b_1 \lesssim 2.5$. This can be contrasted with the halos, which appear in tension with the local Lagrangian model for $b_1 \sim 2$, in agreement with [41, 83]. Finally, we observe a high level of consistency between the hydro galaxies and the HOD/MHQ models.

4.4. Optimal HOD from EFT parameters

We have found excellent agreement between the EFT parameters of hydro galaxies derived from hydrodynamic simulations and those predicted by HOD models. Using the paired distribution of EFT and HOD parameters provided in refs. [35, 36], one can construct a conditional distribution to translate measured EFT parameters from hydrodynamic simulations to the corresponding HOD parameters. This approach offers a computationally inexpensive alternative to directly matching the measured HOD shape in hydrodynamic simulations, enabling a quick estimation of the optimal HOD parameters required to fit hydrodynamic data. To illustrate the utility of this method, we present an example of inferring the HOD parameters needed to reproduce the EFT parameters of hydrodynamical simulations.

To learn the conditional distribution $p(\theta_{\text{HOD}}|\theta_{\text{EFT}})$, we trained a normalizing flow (NF) model using 10,500 mock HOD catalogs generated with **AbacusSummit** N-body simulations, each associated with measured EFT parameters. As a first step, we focus on the paired samples of a HOD-LRG-I model and real space EFT parameters from [35]. The NF model was trained for 40,000 steps, during which validation and training losses were carefully monitored to ensure the absence of overfitting. Upon completion, the NF model effectively captured the intricate relationships between the HOD and EFT parameter spaces, enabling efficient and accurate mapping between them.

Building on the strong agreement between the mea-

sured EFT parameters of hydro galaxies and HOD models demonstrated earlier, no significant domain shift is expected when using hydro galaxy EFT parameters as input. To test this, we sampled the conditional distribution 5,000 times for each input, producing inferred distributions of HOD parameters for MTNG and Astrid. The results are shown in figs. 13 and 14, respectively. Broadly, the generated conditional distributions align well with the HOD priors. However, for Astrid, two samples extend noticeably beyond the priors, likely due to an unresolved degeneracy between the satellite HOD parameters $\log M_1$ and B_{sat} , clearly visible in fig. 14. This example demonstrates the practical utility of the trained normalizing flow model, providing a computationally efficient and robust method for estimating HOD parameters while addressing the challenges of traditional matching techniques.

Note that both for Astrid and MTNG our predictions for the halo mass threshold of centrals $\log M_{\text{cut}}$, and their density-dependent assembly bias parameter B_{cent} are much narrower than the priors. B_{cent} is consistent with zero for all hydro samples. The values of M_{cut} agree well with the halo mass function corresponding to the host halos, see fig. 12.

Beyond LRGs, we have also repeated this analysis using paired samples of the HMQ-ELG model and real-space EFT parameters. In particular, we employed the ELG model from eq. 11, excluding α_s and α_c from the training sample. This approach realizes a mapping from 9 EFT parameters to 12 HOD parameters. After training our NF architecture for 40,000 steps with 10,500 mocks, we generated the inferred distribution of HOD parameters for MTNG and Astrid by conditioning on their measured EFT parameters. These results are shown in figs. 15 and 16, respectively. We find that our results are broadly consistent with the range of priors on HOD parameters used during training. However, it is worth noting that samples without sSFR selection appear somewhat discordant with the prior. This is expected, as such a choice of cut primarily represents LRGs. This is also reflected in the larger values of M_{cut} observed.

5. DISCUSSION

In this work we have studied the accuracy of modeling hydrodynamic galaxies at the field level in the context of

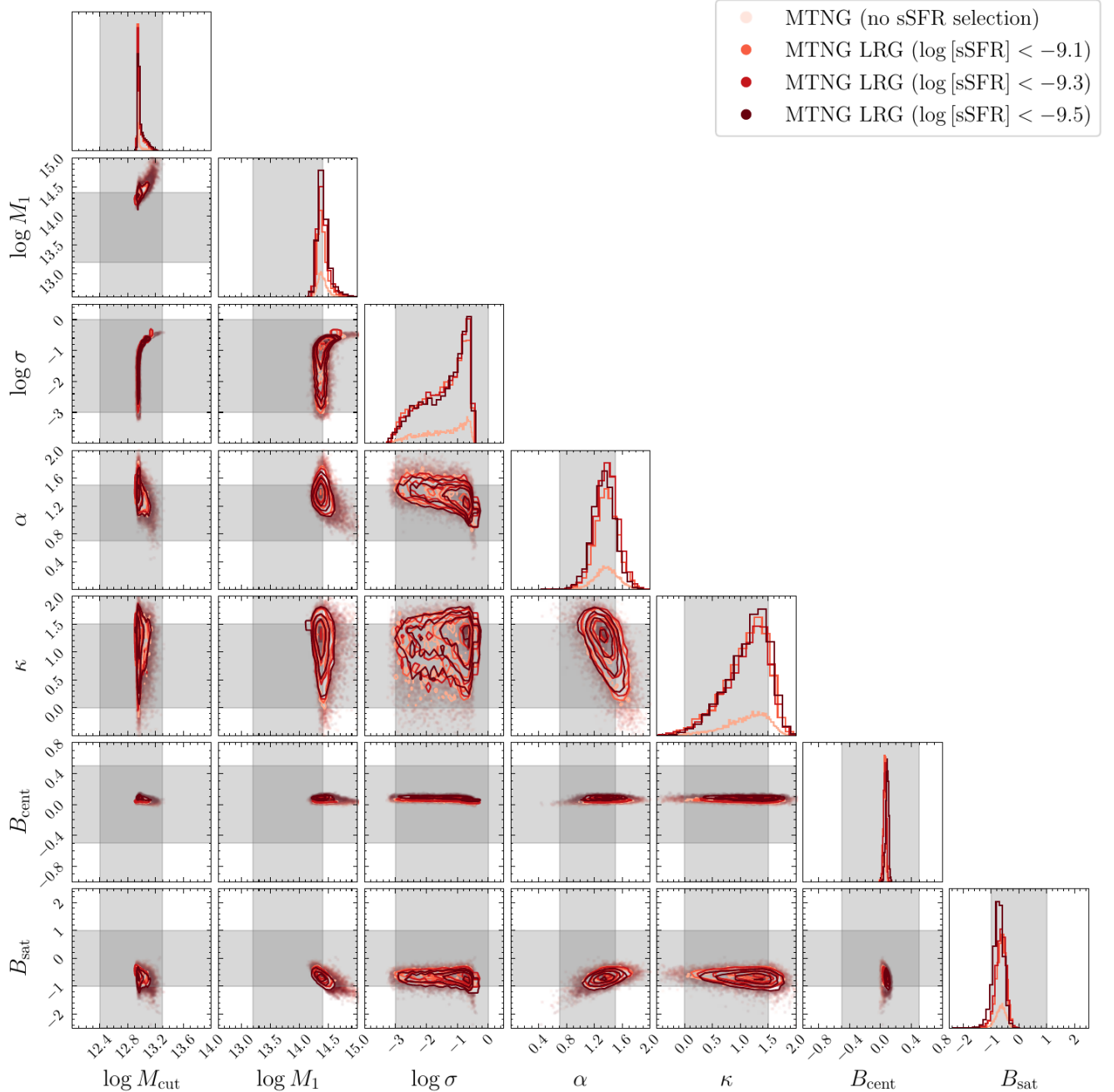


FIG. 13. Inferred distribution of LRG-HOD parameters for MTNG as translated with our learned conditional distribution and using measured EFT parameters. The gray bands represent the range of priors used on HOD parameters in the NF’s training set. See refs. [35, 36] for further details on the underlying data sets.

the EFT forward model. Our main results are summarized in Section 2. Let us now discuss the main extensions of our analysis.

From the theory point of view, it will be interesting to use the semi-analytic galaxy formation approaches, such as [86], to compute the EFT parameters of red and blue galaxies.

It will be important to study the EFT parameters of other types of tracers, such as e.g. the Lyman alpha forest [117, 118], quasars [30], or intrinsic alignments [119]. The latter is particularly important as the hydrodynamic simulation is currently the only robust approach to producing simulation-based priors for intrinsic alignments of galaxies. This work is currently underway.

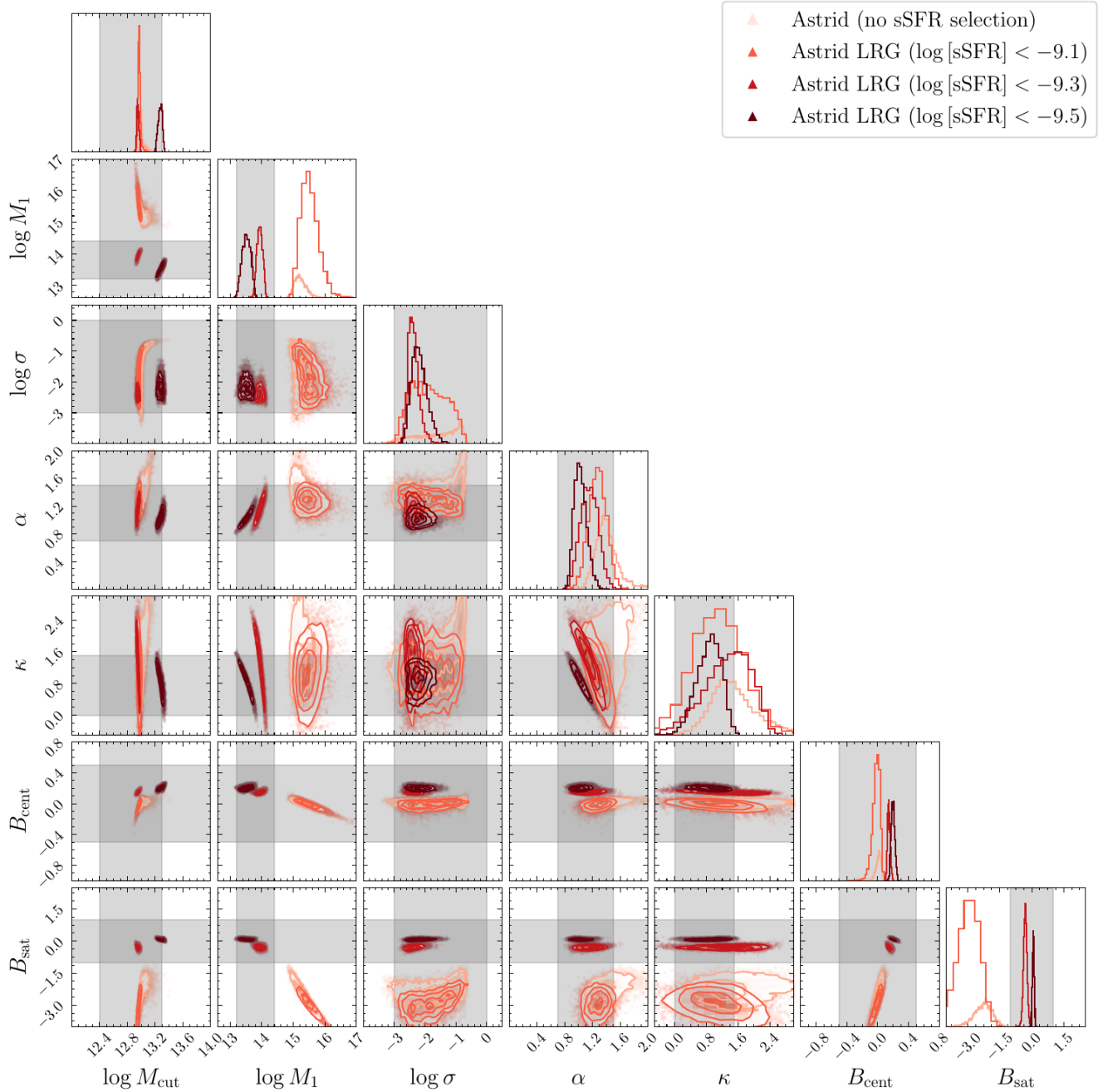


FIG. 14. Same as fig. 13 but for the Astrid simulation.

Our work confirms the validity of the field-level HOD-based priors developed and applied to the BOSS data in [36]. This work has found that the application of HOD-based priors results in a $\sim 5\sigma$ tension with the *Planck* Λ CDM model [96]. Our current study thus reinforces this tension in the BOSS data, which was also independently confirmed with BOSS-CMB lensing cross-correlation data in [31, 120]. It will be interesting to understand the role of EFT/HOD parameters in this ten-

sion.

Finally, it will be important to extend our analysis to other hydrodynamical simulations and other variants of the subgrid models. The ultimate goal of this research direction is to generate priors for EFT-parameters based on different hydrodynamic models. This leaves this and other research directions for future exploration.

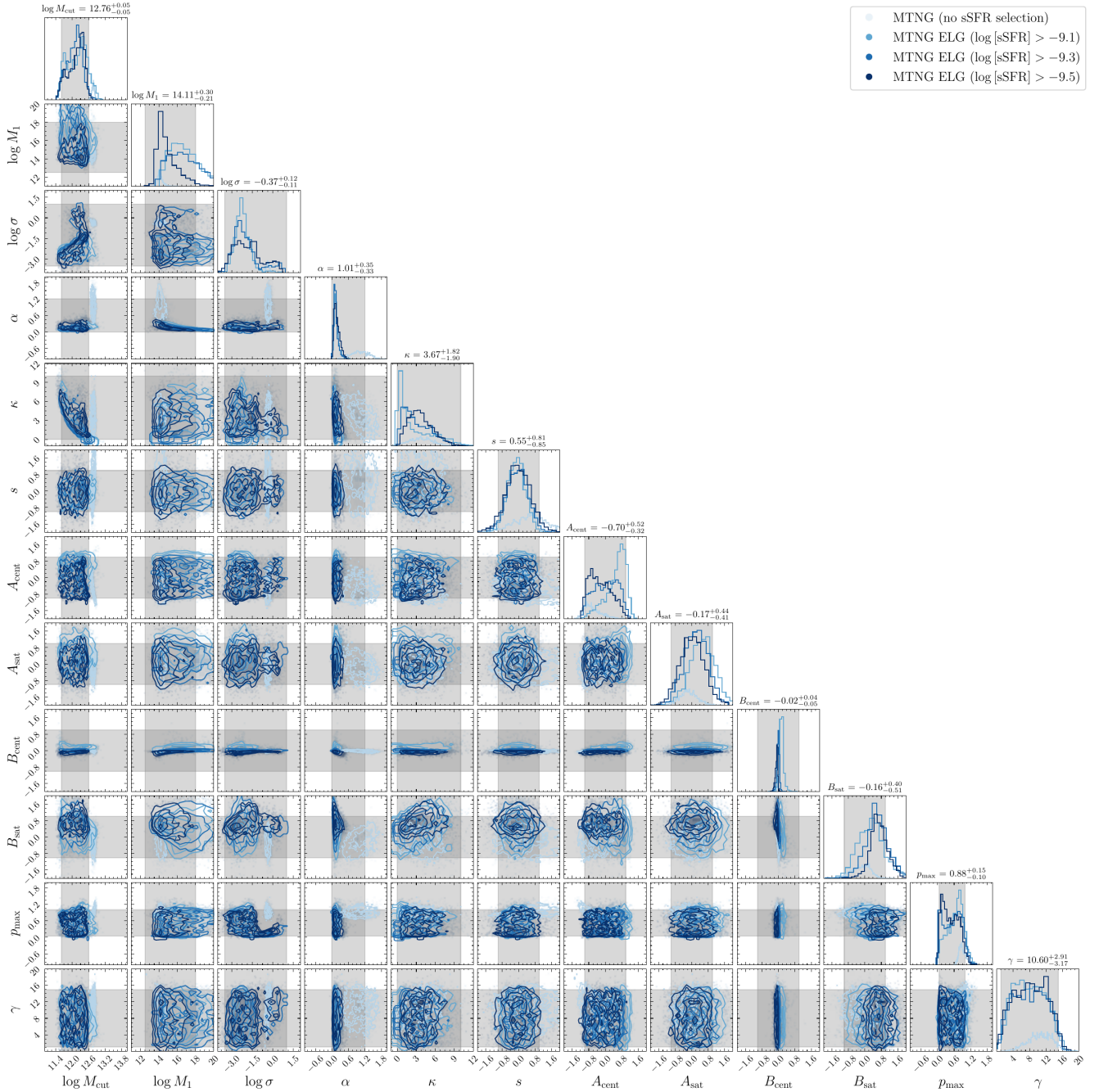


FIG. 15. Inferred distribution of HOD parameters for MTNG ELGs as translated with our learned conditional distribution and using measured EFT parameters. The gray bands represent the range of priors used on HOD parameters in the NF’s training set (Eq. 11).

ACKNOWLEDGMENTS

MI thanks Matias Zaldarriaga for valuable discussions and comments on the draft. This work is supported by the National Science Foundation under Cooperative Agreement PHY-2019786 (The NSF AI Institute for Artificial Intelligence and Fundamental Interactions, <http://iaifi.org/>).

This material is based upon work supported by the U.S. Department of Energy, Office of Science, Office of High Energy Physics of U.S. Department of Energy under grant Contract Number DE-SC0012567. AO acknowledges financial support from the Swiss National Science Foundation (grant no CRSII5_193826). MWT acknowledges financial support from the Simons

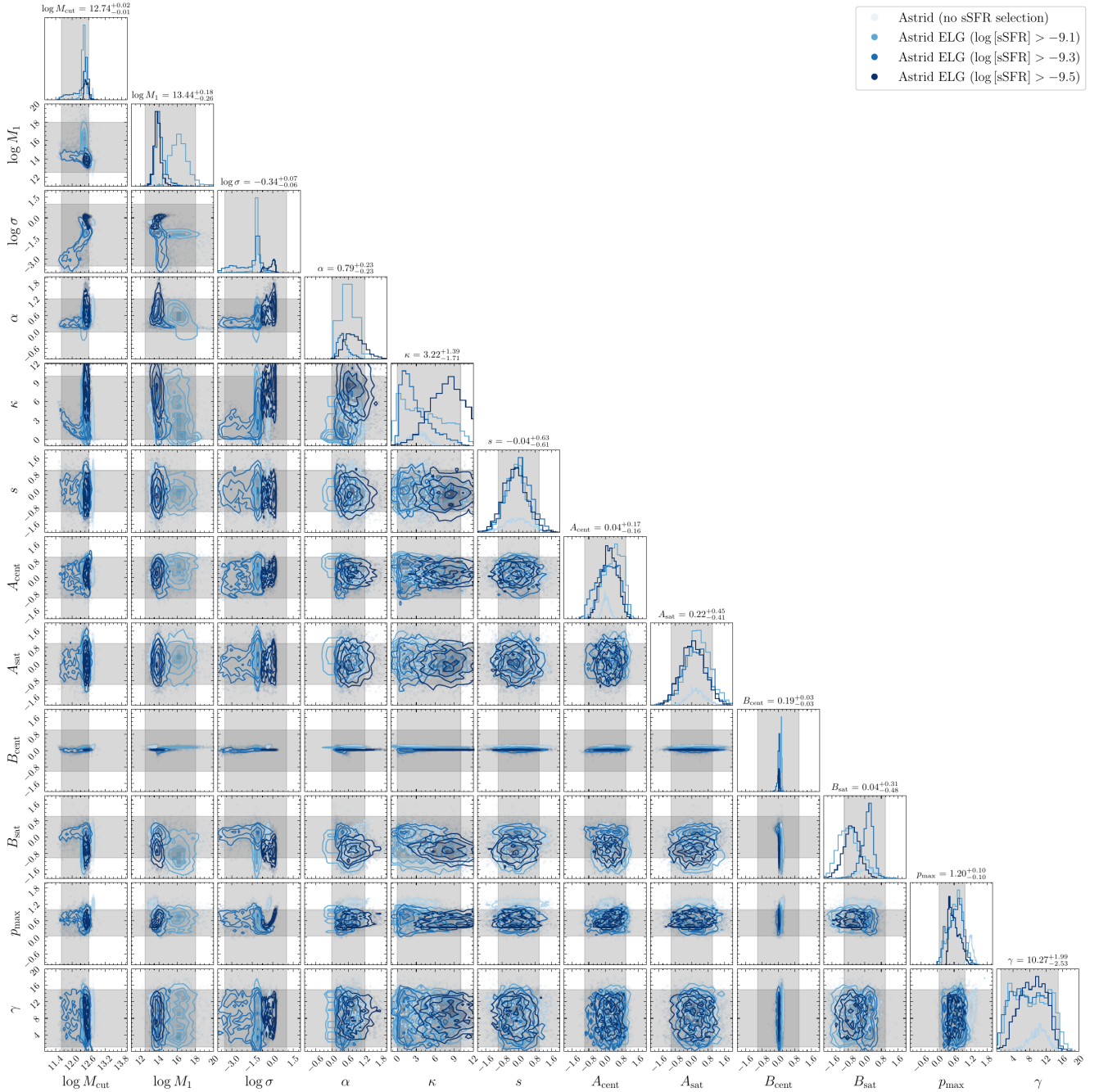


FIG. 16. Same as fig. 15 but for the Astrid simulation.

Foundation (Grant Number 929255). YN is supported by ITC postdoctoral fellowship. CH-A acknowledges support from the Excellence Cluster ORIGINS funded by the Deutsche Forschungsgemeinschaft (DFG, German Research Foundation) under Germany’s Excellence Strategy – EXC-2094 – 390783311. RK acknowledges support of the Natural Sciences and Engineering Research Council of Canada (NSERC) through a Discovery Grant and

a Discovery Launch Supplement (funding reference numbers RGPIN-2024-06222 and DGEGR-2024-00144) and York University’s Global Research Excellence Initiative. LH acknowledges support by the Simons Collaboration on “Learning the Universe”. SB acknowledges funding from a UK Research & Innovation (UKRI) Future Leaders Fellowship [grant number MR/V023381/1].

-
- [1] A. Aghamousa *et al.* (DESI), (2016), [arXiv:1611.00036 \[astro-ph.IM\]](#).
- [2] R. Laureijs *et al.* (EUCLID), (2011), [arXiv:1110.3193 \[astro-ph.CO\]](#).
- [3] v. Ivezić *et al.* (LSST), *Astrophys. J.* **873**, 111 (2019), [arXiv:0805.2366 \[astro-ph\]](#).
- [4] R. Akeson *et al.*, (2019), [arXiv:1902.05569 \[astro-ph.IM\]](#).
- [5] S. Alam *et al.* (eBOSS), *Phys. Rev. D* **103**, 083533 (2021), [arXiv:2007.08991 \[astro-ph.CO\]](#).
- [6] A. G. Adame *et al.* (DESI), (2024), [arXiv:2404.03000 \[astro-ph.CO\]](#).
- [7] I. G. McCarthy, J. Schaye, S. Bird, and A. M. C. Le Brun, *Mon. Not. Roy. Astron. Soc.* **465**, 2936 (2017), [arXiv:1603.02702 \[astro-ph.CO\]](#).
- [8] V. Springel *et al.*, *Mon. Not. Roy. Astron. Soc.* **475**, 676 (2018), [arXiv:1707.03397 \[astro-ph.GA\]](#).
- [9] C. Hernández-Aguayo *et al.*, *Mon. Not. Roy. Astron. Soc.* **524**, 2556 (2023), [arXiv:2210.10059 \[astro-ph.CO\]](#).
- [10] A. A. Berlind, D. H. Weinberg, A. J. Benson, C. M. Baugh, S. Cole, R. Dave, C. S. Frenk, A. Jenkins, N. Katz, and C. G. Lacey, *Astrophys. J.* **593**, 1 (2003), [arXiv:astro-ph/0212357](#).
- [11] Z. Zheng, A. L. Coil, and I. Zehavi, *Astrophys. J.* **667**, 760 (2007), [arXiv:astro-ph/0703457](#).
- [12] A. P. Hearin, A. R. Zentner, F. C. van den Bosch, D. Campbell, and E. Tollerud, *Mon. Not. Roy. Astron. Soc.* **460**, 2552 (2016), [arXiv:1512.03050 \[astro-ph.CO\]](#).
- [13] C. Conroy, R. H. Wechsler, and A. V. Kravtsov, *Astrophys. J.* **647**, 201 (2006), [arXiv:astro-ph/0512234](#).
- [14] R. H. Wechsler and J. L. Tinker, *Ann. Rev. Astron. Astrophys.* **56**, 435 (2018), [arXiv:1804.03097 \[astro-ph.GA\]](#).
- [15] S. Alam, J. A. Peacock, K. Kraljic, A. J. Ross, and J. Comparat (eBOSS), *Mon. Not. Roy. Astron. Soc.* **497**, 581 (2020), [arXiv:1910.05095 \[astro-ph.CO\]](#).
- [16] S. Avila *et al.* (eBOSS), *Mon. Not. Roy. Astron. Soc.* **499**, 5486 (2020), [arXiv:2007.09012 \[astro-ph.CO\]](#).
- [17] S. Yuan, L. H. Garrison, B. Hadzhiyska, S. Bose, and D. J. Eisenstein, *Mon. Not. Roy. Astron. Soc.* **510**, 3301 (2022), [arXiv:2110.11412 \[astro-ph.CO\]](#).
- [18] V. Desjacques, D. Jeong, and F. Schmidt, *Phys. Rept.* **733**, 1 (2018), [arXiv:1611.09787 \[astro-ph.CO\]](#).
- [19] D. Baumann, A. Nicolis, L. Senatore, and M. Zaldarriaga, *JCAP* **1207**, 051 (2012), [arXiv:1004.2488 \[astro-ph.CO\]](#).
- [20] J. J. M. Carrasco, M. P. Hertzberg, and L. Senatore, *JHEP* **09**, 082 (2012), [arXiv:1206.2926 \[astro-ph.CO\]](#).
- [21] M. M. Ivanov, (2022), [arXiv:2212.08488 \[astro-ph.CO\]](#).
- [22] D. Blas, M. Garny, M. M. Ivanov, and S. Sibiryakov, *JCAP* **1607**, 052 (2016), [arXiv:1512.05807 \[astro-ph.CO\]](#).
- [23] D. Blas, M. Garny, M. M. Ivanov, and S. Sibiryakov, *JCAP* **1607**, 028 (2016), [arXiv:1605.02149 \[astro-ph.CO\]](#).
- [24] S.-F. Chen, Z. Vlah, E. Castorina, and M. White, *JCAP* **03**, 100 (2021), [arXiv:2012.04636 \[astro-ph.CO\]](#).
- [25] M. M. Ivanov, M. Simonović, and M. Zaldarriaga, *JCAP* **05**, 042 (2020), [arXiv:1909.05277 \[astro-ph.CO\]](#).
- [26] M. M. Ivanov, M. Simonović, and M. Zaldarriaga, *Phys. Rev. D* **101**, 083504 (2020), [arXiv:1912.08208 \[astro-ph.CO\]](#).
- [27] G. D’Amico, J. Gleyzes, N. Kokron, D. Markovic, L. Senatore, P. Zhang, F. Beutler, and H. Gil-Marín, (2019), [arXiv:1909.05271 \[astro-ph.CO\]](#).
- [28] O. H. E. Philcox and M. M. Ivanov, *Phys. Rev. D* **105**, 043517 (2022), [arXiv:2112.04515 \[astro-ph.CO\]](#).
- [29] S.-F. Chen, Z. Vlah, and M. White, *JCAP* **02**, 008 (2022), [arXiv:2110.05530 \[astro-ph.CO\]](#).
- [30] A. Chudaykin and M. M. Ivanov, (2022), [arXiv:2210.17044 \[astro-ph.CO\]](#).
- [31] S.-F. Chen, M. M. Ivanov, O. H. E. Philcox, and L. Wenzl, (2024), [arXiv:2406.13388 \[astro-ph.CO\]](#).
- [32] F. Beutler *et al.* (BOSS), *Mon. Not. Roy. Astron. Soc.* **466**, 2242 (2017), [arXiv:1607.03150 \[astro-ph.CO\]](#).
- [33] J. M. Sullivan, U. Seljak, and S. Singh, *JCAP* **11**, 026 (2021), [arXiv:2104.10676 \[astro-ph.CO\]](#).
- [34] N. Kokron, J. DeRose, S.-F. Chen, M. White, and R. H. Wechsler, *Mon. Not. Roy. Astron. Soc.* **514**, 2198 (2022), [arXiv:2112.00012 \[astro-ph.CO\]](#).
- [35] M. M. Ivanov, C. Cuesta-Lazaro, S. Mishra-Sharma, A. Obuljen, and M. W. Toomey, *Phys. Rev. D* **110**, 063538 (2024), [arXiv:2402.13310 \[astro-ph.CO\]](#).
- [36] M. M. Ivanov, A. Obuljen, C. Cuesta-Lazaro, and M. W. Toomey, (2024), [arXiv:2409.10609 \[astro-ph.CO\]](#).
- [37] G. Cabass, O. H. E. Philcox, M. M. Ivanov, K. Akitsu, S.-F. Chen, M. Simonović, and M. Zaldarriaga, (2024), [arXiv:2404.01894 \[astro-ph.CO\]](#).
- [38] K. Akitsu, (2024), [arXiv:2410.08998 \[astro-ph.CO\]](#).
- [39] M. Schmittfull, T. Baldauf, and U. Seljak, *Phys. Rev. D* **91**, 043530 (2015), [arXiv:1411.6595 \[astro-ph.CO\]](#).
- [40] T. Lazeyras and F. Schmidt, *JCAP* **1809**, 008 (2018), [arXiv:1712.07531 \[astro-ph.CO\]](#).
- [41] M. M. Abidi and T. Baldauf, *JCAP* **1807**, 029 (2018), [arXiv:1802.07622 \[astro-ph.CO\]](#).
- [42] F. Schmidt, F. Elsner, J. Jasche, N. M. Nguyen, and G. Lavaux, *JCAP* **01**, 042 (2019), [arXiv:1808.02002](#)

- [astro-ph.CO].
- [43] M. Schmittfull, M. Simonović, V. Assassi, and M. Zaldarriaga, *Phys. Rev. D* **100**, 043514 (2019), arXiv:1811.10640 [astro-ph.CO].
- [44] F. Elsner, F. Schmidt, J. Jasche, G. Lavaux, and N.-M. Nguyen, *JCAP* **01**, 029 (2020), arXiv:1906.07143 [astro-ph.CO].
- [45] G. Cabass and F. Schmidt, *JCAP* **04**, 042 (2020), arXiv:1909.04022 [astro-ph.CO].
- [46] C. Modi, S.-F. Chen, and M. White, *Mon. Not. Roy. Astron. Soc.* **492**, 5754 (2020), arXiv:1910.07097 [astro-ph.CO].
- [47] F. Schmidt, (2020), arXiv:2009.14176 [astro-ph.CO].
- [48] F. Schmidt, G. Cabass, J. Jasche, and G. Lavaux, *JCAP* **11**, 008 (2020), arXiv:2004.06707 [astro-ph.CO].
- [49] M. Schmittfull, M. Simonović, M. M. Ivanov, O. H. E. Philcox, and M. Zaldarriaga, *JCAP* **05**, 059 (2021), arXiv:2012.03334 [astro-ph.CO].
- [50] T. Lazeyras, A. Barreira, and F. Schmidt, *JCAP* **10**, 063 (2021), arXiv:2106.14713 [astro-ph.CO].
- [51] A. Obuljen, M. Simonović, A. Schneider, and R. Feldmann, *Phys. Rev. D* **108**, 083528 (2023), arXiv:2207.12398 [astro-ph.CO].
- [52] J. Stadler, F. Schmidt, and M. Reinecke, *JCAP* **10**, 069 (2023), arXiv:2303.09876 [astro-ph.CO].
- [53] N.-M. Nguyen, F. Schmidt, B. Tucci, M. Reinecke, and A. Kostić, (2024), arXiv:2403.03220 [astro-ph.CO].
- [54] S. Foreman, A. Obuljen, and M. Simonović, (2024), arXiv:2405.18559 [astro-ph.CO].
- [55] M. M. Ivanov, O. H. E. Philcox, T. Nishimichi, M. Simonović, M. Takada, and M. Zaldarriaga, *Phys. Rev. D* **105**, 063512 (2022), arXiv:2110.10161 [astro-ph.CO].
- [56] M. M. Ivanov, O. H. E. Philcox, M. Simonović, M. Zaldarriaga, T. Nishimichi, and M. Takada, *Phys. Rev. D* **105**, 043531 (2022), arXiv:2110.00006 [astro-ph.CO].
- [57] A. Barreira, T. Lazeyras, and F. Schmidt, *JCAP* **08**, 029 (2021), arXiv:2105.02876 [astro-ph.CO].
- [58] R. Pakmor *et al.*, *Mon. Not. Roy. Astron. Soc.* **524**, 2539 (2023), arXiv:2210.10060 [astro-ph.CO].
- [59] S. Alam *et al.* (BOSS), *Mon. Not. Roy. Astron. Soc.* **470**, 2617 (2017), arXiv:1607.03155 [astro-ph.CO].
- [60] S. Bird, Y. Ni, T. Di Matteo, R. Croft, Y. Feng, and N. Chen, *Mon. Not. Roy. Astron. Soc.* **512**, 3703 (2022), arXiv:2111.01160.
- [61] Y. Ni, N. Chen, Y. Zhou, M. Park, Y. Yang, T. DiMatteo, S. Bird, and R. Croft, arXiv e-prints, arXiv:2409.10666 (2024), arXiv:2409.10666 [astro-ph.GA].
- [62] B. Hadzhiyska, S. Tacchella, S. Bose, and D. J. Eisenstein, *Mon. Not. Roy. Astron. Soc.* **502**, 3599 (2021), arXiv:2011.05331 [astro-ph.GA].
- [63] B. Hadzhiyska *et al.*, *Mon. Not. Roy. Astron. Soc.* **524**, 2507 (2023), arXiv:2210.10072 [astro-ph.CO].
- [64] B. Hadzhiyska *et al.*, *Mon. Not. Roy. Astron. Soc.* **524**, 2524 (2023), arXiv:2210.10068 [astro-ph.CO].
- [65] S. Bose *et al.*, *Mon. Not. Roy. Astron. Soc.* **524**, 2579 (2023), arXiv:2210.10065 [astro-ph.CO].
- [66] S. Yuan, D. J. Eisenstein, and L. H. Garrison, *Mon. Not. Roy. Astron. Soc.* **478**, 2019 (2018), arXiv:1802.10115 [astro-ph.CO].
- [67] E. Krause *et al.* (Beyond-2pt), (2024), arXiv:2405.02252 [astro-ph.CO].
- [68] G. Valogiannis, S. Yuan, and C. Dvorkin, *Phys. Rev. D* **109**, 103503 (2024), arXiv:2310.16116 [astro-ph.CO].
- [69] J. Hou, A. Moradinezhad Dizgah, C. Hahn, M. Eickenberg, S. Ho, P. Lemos, E. Massara, C. Modi, L. Parker, and B. R.-S. Blancard, *Phys. Rev. D* **109**, 103528 (2024), arXiv:2401.15074 [astro-ph.CO].
- [70] C. Hahn *et al.*, (2023), arXiv:2310.15246 [astro-ph.CO].
- [71] B. R.-S. Blancard *et al.* (SimBIG), *Phys. Rev. D* **109**, 083535 (2024), arXiv:2310.15250 [astro-ph.CO].
- [72] P. Lemos *et al.* (SimBIG), *Phys. Rev. D* **109**, 083536 (2024), arXiv:2310.15256 [astro-ph.CO].
- [73] C. Hahn, M. Eickenberg, S. Ho, J. Hou, P. Lemos, E. Massara, C. Modi, A. Moradinezhad Dizgah, L. Parker, and B. R.-S. Blancard (SimBIG), *Phys. Rev. D* **109**, 083534 (2024), arXiv:2310.15243 [astro-ph.CO].
- [74] F. G. Mohammad *et al.*, *Astron. Astrophys.* **610**, A59 (2018), arXiv:1708.00026 [astro-ph.CO].
- [75] A. de Mattia *et al.* (eBOSS), *Mon. Not. Roy. Astron. Soc.* **501**, 5616 (2021), arXiv:2007.09008 [astro-ph.CO].
- [76] M. M. Ivanov, (2021), arXiv:2106.12580 [astro-ph.CO].
- [77] A. G. Adame *et al.* (DESI), (2024), arXiv:2411.12021 [astro-ph.CO].
- [78] A. Chudaykin and M. M. Ivanov, *JCAP* **11**, 034 (2019), arXiv:1907.06666 [astro-ph.CO].
- [79] N. Sailer, E. Castorina, S. Ferraro, and M. White, *JCAP* **12**, 049 (2021), arXiv:2106.09713 [astro-ph.CO].
- [80] S. Yuan *et al.* (DESI), (2023), arXiv:2310.09329 [astro-ph.CO].
- [81] C. Garcia-Quintero *et al.* (DESI), (2024), arXiv:2404.03009 [astro-ph.CO].
- [82] A. Rocher *et al.*, *JCAP* **10**, 016 (2023), arXiv:2306.06319 [astro-ph.CO].
- [83] A. Eggemeier, R. Scoccimarro, R. E. Smith, M. Crocce, A. Pezzotta, and A. G. Sánchez, (2021), arXiv:2102.06902 [astro-ph.CO].
- [84] T. Lazeyras, C. Wagner, T. Baldauf, and F. Schmidt, *JCAP* **1602**, 018 (2016), arXiv:1511.01096 [astro-ph.CO].
- [85] S. Alam *et al.* (eBOSS), (2020), 10.1093/mnras/stab1150, arXiv:2007.09004 [astro-ph.CO].

- [86] M. Marinucci, V. Desjacques, and A. Benson, (2023), [10.1093/mnras/stad1884](https://arxiv.org/abs/10.1093/mnras/stad1884), [arXiv:2303.10337](https://arxiv.org/abs/2303.10337) [astro-ph.CO].
- [87] J. C. Jackson, *Mon. Not. Roy. Astron. Soc.* **156**, 1P (1972), [arXiv:0810.3908](https://arxiv.org/abs/0810.3908) [astro-ph].
- [88] F. Villaescusa-Navarro *et al.* (CAMELS), *Astrophys. J.* **915**, 71 (2021), [arXiv:2010.00619](https://arxiv.org/abs/2010.00619) [astro-ph.CO].
- [89] R. Weinberger, V. Springel, L. Hernquist, A. Pillepich, F. Marinacci, R. Pakmor, D. Nelson, S. Genel, M. Vogelsberger, J. Naiman, and P. Torrey, *MNRAS* **465**, 3291 (2017), [arXiv:1607.03486](https://arxiv.org/abs/1607.03486) [astro-ph.GA].
- [90] A. Pillepich *et al.*, *Mon. Not. Roy. Astron. Soc.* **473**, 4077 (2018), [arXiv:1703.02970](https://arxiv.org/abs/1703.02970) [astro-ph.GA].
- [91] D. Nelson *et al.*, *Mon. Not. Roy. Astron. Soc.* **475**, 624 (2018), [arXiv:1707.03395](https://arxiv.org/abs/1707.03395) [astro-ph.GA].
- [92] J. P. Naiman, A. Pillepich, V. Springel, E. Ramirez-Ruiz, P. Torrey, M. Vogelsberger, R. Pakmor, D. Nelson, F. Marinacci, L. Hernquist, R. Weinberger, and S. Genel, *MNRAS* **477**, 1206 (2018), [arXiv:1707.03401](https://arxiv.org/abs/1707.03401) [astro-ph.GA].
- [93] F. Marinacci, M. Vogelsberger, R. Pakmor, P. Torrey, V. Springel, L. Hernquist, D. Nelson, R. Weinberger, A. Pillepich, J. Naiman, and S. Genel, *MNRAS* **480**, 5113 (2018), [arXiv:1707.03396](https://arxiv.org/abs/1707.03396) [astro-ph.CO].
- [94] D. Nelson, A. Pillepich, V. Springel, R. Pakmor, R. Weinberger, S. Genel, P. Torrey, M. Vogelsberger, F. Marinacci, and L. Hernquist, *Mon. Not. Roy. Astron. Soc.* **490**, 3234 (2019), [arXiv:1902.05554](https://arxiv.org/abs/1902.05554) [astro-ph.GA].
- [95] A. Pillepich, D. Nelson, V. Springel, R. Pakmor, P. Torrey, R. Weinberger, M. Vogelsberger, F. Marinacci, S. Genel, A. van der Wel, and L. Hernquist, *MNRAS* **490**, 3196 (2019), [arXiv:1902.05553](https://arxiv.org/abs/1902.05553) [astro-ph.GA].
- [96] Planck Collaboration, N. Aghanim, and A. Zonca, *A&A* **641**, A6 (2020), [arXiv:1807.06209](https://arxiv.org/abs/1807.06209) [astro-ph.CO].
- [97] N. Katz, D. H. Weinberg, and L. Hernquist, *ApJS* **105**, 19 (1996), [arXiv:astro-ph/9509107](https://arxiv.org/abs/astro-ph/9509107) [astro-ph].
- [98] M. Vogelsberger, S. Genel, V. Springel, P. Torrey, D. Sijacki, D. Xu, G. Snyder, D. Nelson, and L. Hernquist, *MNRAS* **444**, 1518 (2014), [arXiv:1405.2921](https://arxiv.org/abs/1405.2921) [astro-ph.CO].
- [99] N. Battaglia, H. Trac, R. Cen, and A. Loeb, *ApJ* **776**, 81 (2013), [arXiv:1211.2821](https://arxiv.org/abs/1211.2821) [astro-ph.CO].
- [100] C.-A. Faucher-Giguère, *MNRAS* **493**, 1614 (2020), [arXiv:1903.08657](https://arxiv.org/abs/1903.08657) [astro-ph.CO].
- [101] A. Rahmati, A. H. Pawlik, M. Raičević, and J. Schaye, *MNRAS* **430**, 2427 (2013), [arXiv:1210.7808](https://arxiv.org/abs/1210.7808) [astro-ph.CO].
- [102] V. Springel and L. Hernquist, *MNRAS* **339**, 289 (2003), [arXiv:astro-ph/0206393](https://arxiv.org/abs/astro-ph/0206393) [astro-ph].
- [103] M. R. Krumholz and N. Y. Gnedin, *ApJ* **729**, 36 (2011), [arXiv:1011.4065](https://arxiv.org/abs/1011.4065) [astro-ph.CO].
- [104] T. Okamoto, C. S. Frenk, A. Jenkins, and T. Theuns, *MNRAS* **406**, 208 (2010), [arXiv:0909.0265](https://arxiv.org/abs/0909.0265) [astro-ph.CO].
- [105] Y. Ni, T. Di Matteo, S. Bird, R. Croft, Y. Feng, N. Chen, M. Tremmel, C. DeGraf, and Y. Li, *MNRAS* **513**, 670 (2022), [arXiv:2110.14154](https://arxiv.org/abs/2110.14154) [astro-ph.GA].
- [106] S. Pandey, K. Lehman, E. J. Baxter, Y. Ni, D. Anglés-Alcázar, S. Genel, F. Villaescusa-Navarro, A. M. Delgado, and T. di Matteo (CAMELS), *Mon. Not. Roy. Astron. Soc.* **525**, 1779 (2023), [arXiv:2301.02186](https://arxiv.org/abs/2301.02186) [astro-ph.CO].
- [107] N. A. Maksimova, L. H. Garrison, D. J. Eisenstein, B. Hadzhiyska, S. Bose, and T. P. Satterthwaite, *Mon. Not. Roy. Astron. Soc.* **508**, 4017 (2021), [arXiv:2110.11398](https://arxiv.org/abs/2110.11398) [astro-ph.CO].
- [108] H. Guo, Z. Zheng, I. Zehavi, K. Dawson, R. A. Skibba, J. L. Tinker, D. H. Weinberg, M. White, and D. P. Schneider (BOSS), *Mon. Not. Roy. Astron. Soc.* **446**, 578 (2015), [arXiv:1407.4811](https://arxiv.org/abs/1407.4811) [astro-ph.CO].
- [109] E. Paillas *et al.*, (2023), [arXiv:2309.16541](https://arxiv.org/abs/2309.16541) [astro-ph.CO].
- [110] B. Hadzhiyska, D. Eisenstein, S. Bose, L. H. Garrison, and N. Maksimova, *Mon. Not. Roy. Astron. Soc.* **509**, 501 (2021), [arXiv:2110.11408](https://arxiv.org/abs/2110.11408) [astro-ph.CO].
- [111] M. Davis, G. Efstathiou, C. S. Frenk, and S. D. M. White, *APJ* **292**, 371 (1985).
- [112] P. S. Behroozi, R. H. Wechsler, and H.-Y. Wu, *APJ* **762**, 109 (2013), [arXiv:1110.4372](https://arxiv.org/abs/1110.4372) [astro-ph.CO].
- [113] S. Yuan, B. Hadzhiyska, S. Bose, and D. J. Eisenstein, *Mon. Not. Roy. Astron. Soc.* **512**, 5793 (2022), [arXiv:2202.12911](https://arxiv.org/abs/2202.12911) [astro-ph.CO].
- [114] T. Baldauf, U. Seljak, V. Desjacques, and P. McDonald, *Phys. Rev. D* **86**, 083540 (2012), [arXiv:1201.4827](https://arxiv.org/abs/1201.4827) [astro-ph.CO].
- [115] F. Villaescusa-Navarro *et al.*, *Astrophys. J. Suppl.* **250**, 2 (2020), [arXiv:1909.05273](https://arxiv.org/abs/1909.05273) [astro-ph.CO].
- [116] J. L. Tinker, B. E. Robertson, A. V. Kravtsov, A. Klypin, M. S. Warren, G. Yepes, and S. Gottlober, *Astrophys. J.* **724**, 878 (2010), [arXiv:1001.3162](https://arxiv.org/abs/1001.3162) [astro-ph.CO].
- [117] M. M. Ivanov, *Phys. Rev. D* **109**, 023507 (2024), [arXiv:2309.10133](https://arxiv.org/abs/2309.10133) [astro-ph.CO].
- [118] M. M. Ivanov, M. W. Toomey, and N. G. Karaçaylı, (2024), [arXiv:2405.13208](https://arxiv.org/abs/2405.13208) [astro-ph.CO].
- [119] S. Chen *et al.*, (2024), [arXiv:2407.04795](https://arxiv.org/abs/2407.04795) [astro-ph.CO].
- [120] S.-F. Chen, M. White, J. DeRose, and N. Kokron, *JCAP* **07**, 041 (2022), [arXiv:2204.10392](https://arxiv.org/abs/2204.10392) [astro-ph.CO].